Article

The first emergence of unprecedented global water scarcity in the Anthropocene

Vecchia P. Ravinandrasana [1,2] & Christian L. E. Franzke [1,2] ✉

Access to water is crucial for all aspects of life. Anthropogenic global warming is projected to disrupt the hydrological cycle, leading to water scarcity. However, the timing and hotspot regions of unprecedented water scarcity are unknown. Here, we estimate the Time of First Emergence (ToFE) of drought-driven water scarcity events, referred to as "Day Zero Drought" (DZD), which arises from hydrological compound extremes, including prolonged rainfall deficits, reduced river flow, and increasing water consumption. Using a probabilistic framework and a large ensemble of climate simulations, we attribute the timing and likelihood of DZD events to human influence. Many regions, including major reservoirs, may face high risk of DZD by the 2020s and 2030s. Despite model and scenario uncertainties, consistent DZD hotspots emerge across the Mediterranean, southern Africa, and parts of North America. Urban populations are particularly vulnerable at the 1.5 °C warming level. The length of time between successive DZD events is shorter than the duration of DZD, limiting recovery periods and exacerbating water scarcity risks. Therefore, more proactive water strategies are urgently needed to avoid severe societal impacts of DZD.

In late 2017 and early 2018, the city of Cape Town, South Africa, was threatened by an unprecedented water scarcity crisis, known as "Day Zero Drought" (DZD), triggered by an exceptional 3-year rainfall deficit that started in 2015[1]. This event was characterized by the lowest river flows recorded since 1904[2] in the Sonderend River and drained the largest reservoir[3], Theewaterskloof, to critical levels. The vulnerability and scale of the population exposure made it one of the most extreme multi-year droughts on record, leading to severe water restrictions and socio-economic consequences[4,5]. The long duration of the drought and the high water demand made the situation dire, especially for a city relying for 96% on surface water and only 4% on groundwater[6]. Although Cape Town ultimately avoided reaching DZD, due to the slightly above-average rainfall in winter 2018 and subsequent wetter years, this event remains the major urban drought in recent history. Similar crises occurred in cities like Chennai in 2019[7], while other cities like Los Angeles[8] remain highly vulnerable. These cases highlight the growing global concern over urban water security and serve as a wake-up call to the risks of water insecurity.

Traditional droughts, meteorological, agricultural, and hydrological, are typically assessed in isolation based on deficits in precipitation, soil moisture, or streamflow. In contrast, water scarcity is a multidimensional event arising from insufficient quantity, compromised quality, and unmet environmental flow requirements, constraining the sustainable availability of water sources for human and ecological systems[9]. This study focuses on socio-physical water scarcity, driven by anthropogenic supply-demand imbalances. However, DZD represents an acute water scarcity triggered by the simultaneous occurrence of multi-year precipitation deficits, river flow depletion, and high-water demand, leading to a critical depletion of reservoirs. Therefore, DZD is a multi-year compound extreme event arising from the concurrent occurrence of several interdependent events[10]. A compound extreme event refers to a simultaneous occurrence of multiple extreme events that can have drastic effects on a large scale, far greater than the impact of an individual event[11,12]. Multi-year meteorological drought, driven by insufficient precipitation and potentially exacerbated by global warming, can lead to hydrological

[1]Center for Climate Physics, Institute for Basic Science, Busan, Republic of Korea. [2]Department of Integrated Climate System Science, Pusan National University, Busan, Republic of Korea. ✉e-mail: christian.franzke@pusan.ac.kr

droughts characterized by abnormally low river flows, reducing water availability. Such combined events considerably increase the risk of water scarcity when the available supply is less than the demand. Hence, the simultaneous occurrence of several climate extremes can lead to more severe impacts[13] on water supply[14] and subsequently on society and ecosystems[15], highlighting the need for integrated drought assessment frameworks that account for compound events.

Intensive water consumption due to economic development, population growth, and modern agriculture, heightens the risk that water resources, depleted by drought, will not be able to meet sectoral water demands. On a global level, future climate projections indicate that global warming is expected to disrupt and intensify the water cycle variability[16], leading to more severe wet-dry fluctuation periods[17], enhancing evapotranspiration[18], and reducing precipitation and surface runoff[16] in many regions. These changes are expected to increase the likelihood of both climatological and hydrological water stress[19–22]. Despite the distinct nature of drought and water scarcity, their relationship is crucial in the hydrological system[23]. Climate change and socioeconomic development drive global freshwater scarcity[24–26], affecting numerous populations[27]. However, the risk of future global water scarcity, caused by anthropogenic climate change and rising water demand across all sectors, and its impacts[28,29] remain poorly understood due to the complexity of its socio-economic and physical interactions.

Few studies have focused on understanding the DZD drivers, and then mainly for Cape Town, South Africa[1,2,4,30–33]. The event was caused by a wet-season rainfall deficit and long-term decline in the frequency and intensity of rainy days, making the rainy season shorter than the dry season[34,35]. Anthropogenic climate change contributed to DZD[36,37] and is expected to increase its future likelihood[33]. However, global-scale assessments of the emergence and attribution of DZD-like events under global warming remain limited. Understanding where and when such compound events will emerge is crucial for local and global water security strategies.

To the best of our knowledge, few studies have assessed the Time of First Emergence (ToFE) of extreme events such as unprecedented hydrological drought[38] and water scarcity[39], under human-induced climate change. For instance, Liu et al.[39] estimated the ToFE of water scarcity and its potential disappearance based on a per-capita water availability metric. However, the understanding of ToFE of water scarcity driven by the compound effects of hydrological drought and socio-economic growth remains limited. Here, water scarcity arises when freshwater demand exceeds the available supply, including reservoir storage, under compound drought conditions. Reservoirs are essential for managing local water availability and assessing the severity of water scarcity under climate change[40]. However, reservoir feedback[41,42] due to reservoir dependence can increase vulnerability to water shortages during prolonged drought, as increased storage capacity encourages greater water consumption. Reservoirs help mitigate hydrological extremes, but over-reliance can mask water stress and delay adaptation strategies. Therefore, there is an urgent need for in-depth research on reservoir-related water security risks to achieve water-related sustainable development goals.

This study assesses the characteristics of global physical water scarcity caused by hydrological drought in anthropogenic climate change using a probabilistic framework based on large-ensemble model simulations. Our study specifically addresses water scarcity that arises when prolonged drought reduces water supply below demand. To investigate the emergence of extreme drought-driven water scarcity, we use 100 ensemble members of climate projections with the Community Earth System Model version 2 Large Ensemble (CESM2-LE) under the SSP3-7.0 scenario for probabilistic analysis. We also include the Centre National de Recherches Météorologiques (CNRM) model under SSP3-7.0 and SSP2-4.5 scenarios for the sensitivity of our results,

using 10 ensemble members for each scenario to ensure consistency. The CNRM-based analysis is solely for the sensitivity of the ToFE due to its coarser spatial resolution relative to CESM2-LE. We evaluate the global ToFE of prolonged drought-driven water scarcity, such as DZD, using a method based on the Fraction of Attributable Risk (FAR) of the joint probability of compound extremes, incorporating reservoir and lake levels. We apply the FAR to quantify the increase in the likelihood of DZD events due to human-induced climate change, attributing the risk to the anthropogenic forcing. Our study focuses on DZD as an acute water scarcity event due to a long period of unprecedented compound extreme events in water supply shortage and rising demand under a warming climate. We identify when and where anthropogenic DZD first emerges, how long these events will last, and how many people will be exposed to DZD.

Results
Emergence of multi-year drought due to anthropogenic global warming

We investigate drought-driven water scarcity as a compound extreme event characterized by the concurrent exceedance of thresholds of four indicators: the 48-month Standardized Precipitation Evapotranspiration Index (SPEI48), the Standardized River Flow Index (SRFI48), and the Standardized Water Scarcity Index (SWSI48), as illustrated in Fig. 1, and Time for Reservoirs to Dry (TRD, Supplementary Fig. 6). Although SPEI is widely used for capturing atmospheric water demand through Potential Evapotranspiration (PET), it does not reflect actual water losses from the land surface, which actual evapotranspiration better represents. Nonetheless, PET-based indices remain suitable for detecting climate-driven drought in long-term, large-scale studies due to their broader data availability and methodology.

Our results quantify the spatial distributions of water stress and suggest that some regions will encounter unprecedented regional drought conditions due to global warming under the SSP3-7.0 scenario (Fig. 1). Regarding the SPEI48 and SRFI48 indices, most regions are expected to experience unprecedented severe multi-year hydrological droughts, especially towards the end of the twenty-first century under anthropogenic climate change. SWSI48 shows the emergence of regional water scarcity in future periods.

Towards the end of the twenty-first century, almost all regions are at high risk of severe and pronounced persistent drought (i.e., SPEI48, Fig. 1c) in the far future. Our findings align with a previous study[43] indicating a persistent increase in severe multi-year drought in the future over southern Africa, northern South America, the Mediterranean Region, Australia, and Chile. Conversely, regions like Argentina, East Africa, and high-latitude Russia are projected to experience wetter climates.

Similarly, the spatial distribution of SRFI48 (Fig. 1e, f) indicates an increase and intensification of severe multi-year river flow extremes in the future[44]. This is projected to intensify in the far future[45,46]. A substantial decline in the Yangtze River water level is projected in the near future, followed by a slight increase in the far future. The increase in streamflow in the far future is driven by increased snowmelt[47,48] and precipitation[49], which could lead to water level rises. Notably, anthropogenic climate change is projected to also alter the world's largest river flow systems, such as the Amazon River. However, an increase of a high risk of the occurrence of extreme floods[50] is projected in the far future for the biggest rivers, such as the Rio de la Plata, Nile, Congo, and Yellow Rivers.

The SWSI48 addresses the multi-year impact of increasing water demand with a decrease in water supply in a warming world. Our results show the emergence of acute water scarcity in the future (Fig. 1h, i), with total water demand exceeding total water supply. The expansion of regions impacted by water scarcity shows the intensification of SWSI48, particularly in the western United States of America,

Mediterranean regions, northern Africa, southern Africa, India, northern China, and southern Australia.

Consequently, our results state that several regions will at the same time encounter severe dryness, as indicated by SPEI48 less than −1.5, persistent reduction in river discharge, by SRFI48 less than −1.5, and chronic acute water scarcity, defined by SWSI48 less than 0.6. Therefore, these simultaneous occurrences of multiple water-related stress factors driven by long-duration rainfall deficits, increased evapotranspiration, depleted river flow, and increased water consumption are projected to intensify jointly under a warming climate scenario, CESM2-LE SSP3.7-0. This compound pattern of multi-year water stress underscores an increasing prevalence of extreme water stress[26,38,45,51] and scarcity[52] in the future, especially in already drought-prone regions.

Time of First Emergence (ToFE) of DZD
This study defines ToFE as the first decade in which the Fraction of Attributable Risk (FAR) for DZD exceeds 0.99, indicating a 99% likelihood that human activities caused the onset of these unprecedented compound drought-scarcity events. ToFE is assessed relative to pre-industrial conditions (1850–1899), which serve as the baseline for detecting anthropogenic emergence. The focal hotspot regions affected by unprecedented DZD, with their respective decade of ToFE and the distribution of the ToFE, are shown in Fig. 2. Our results indicate that anthropogenic climate change is projected to trigger the onset and occurrence of DZD, primarily due to severe and persistent compound multi-year hydrological droughts, reservoir depletion, and high-water demand.

About 14% of the global reservoirs from the Global Reservoir and Dams (GRand) database (Supplementary Fig. 5, see Methods for more information regarding the reservoirs) would dry out due to a high risk of DZD during their respective ToFE, as shown in Fig. 2a. The 74% of regions covered by DZD are projected to experience an unprecedented water scarcity by 2100, under the SSP3-7.0 scenario of CESM2-LE. Moreover, almost 35% of those regions are facing the emergence of water scarcity, including their reservoirs, between 2020 and 2030 (Fig. 2b). This will threaten the local freshwater availability in DZD-prone regions (Supplementary Fig. 7). Declining precipitation and river flows, combined with rising water demand, can dry up the reservoirs and cause water scarcity across sectors, heightening the risks of water, food, or socio-economic insecurity.
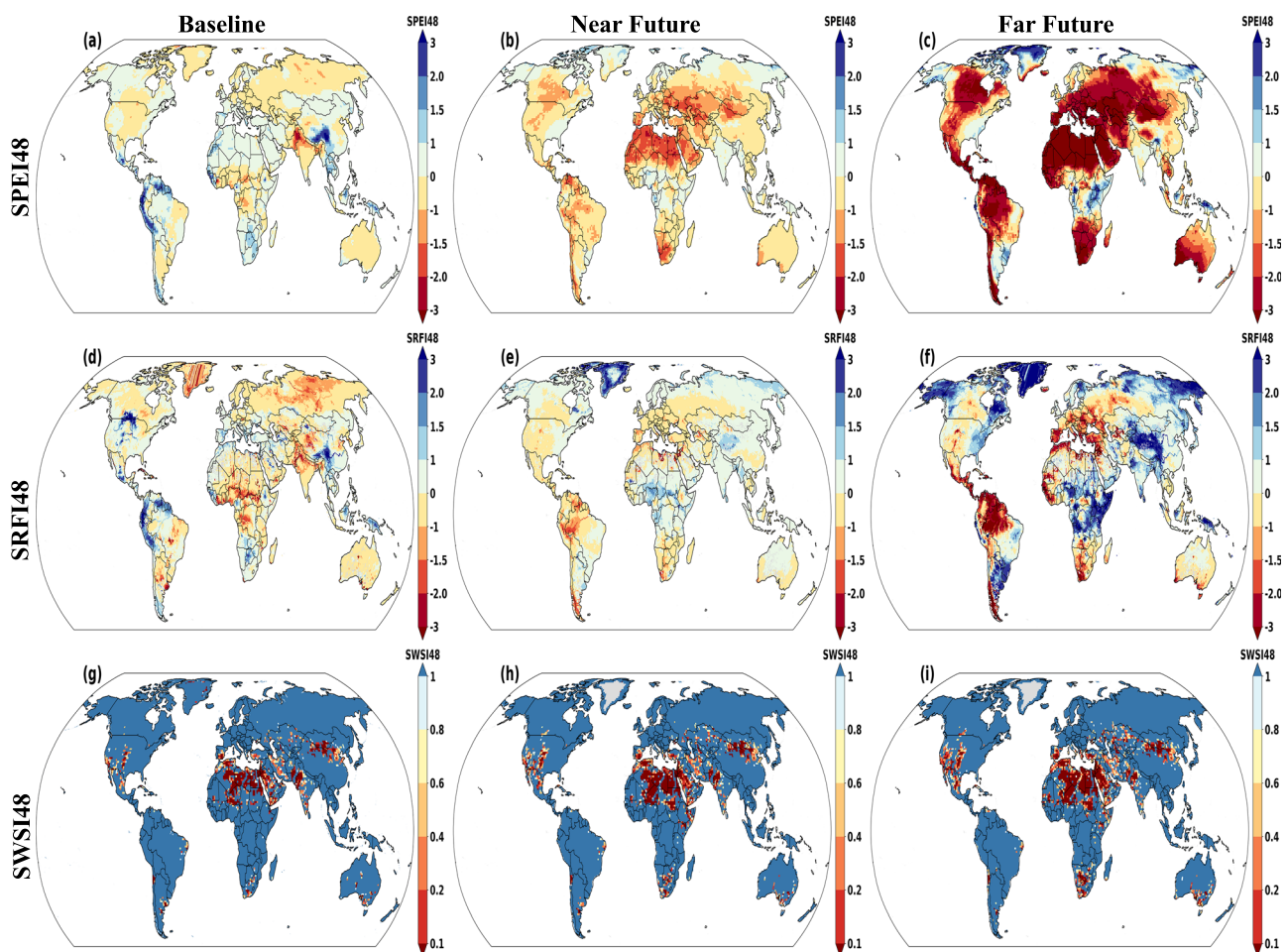

Fig. 1 | Ensemble mean of drought-related and water scarcity indices at a 48-month timescale across three time periods based on CESM2-LE simulations. The first column panel shows the ensemble mean of water stress for the pre-industrial period (1850–1899), which is considered as the baseline period, the second column panel for the near future (2020–2050), and the third column panel for the far future (2070–2100). **a**–**c** Present the Standardized Precipitation-Evapotranspiration Index (SPEI48), indicating long-term climatic water balance at a 48-month timescale. **d**–**f** Show the Standardized River Flow Index (SRFI48), capturing hydrological drought conditions at a 48-month timescale. **g**–**i** Depict the Standardized Water Scarcity Index (SWSI48), reflecting the ratio of total water supply to total water consumption at a 48-month timescale. Each panel represents the ensemble mean, illustrating the spatial pattern and severity of compound water stress indicators over time. Negative values of SPEI48 and SRFI48 indicate increasingly dry conditions, while lower SWSI48 values (i.e., supply-to-demand ratios below normal) signal intensifying water scarcity driven by growing demand. Together, these projections reveal areas at high risk of compound, long-term water stress under future climate and socio-economic scenarios.
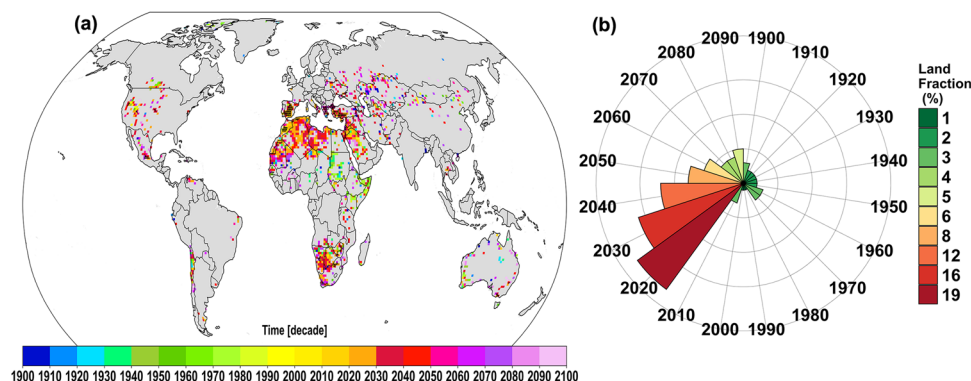
Fig. 2 | Time of First Emergence (ToFE) of Day Zero Drought (DZD) event and global hotspot regions based on CESM2-LE ensemble simulations under the SSP3-7.0 scenario. a Spatial distribution of the decadal ToFE of DZD events across the globe from 1900 to 2100. Colored shading indicates the first decade during which DZD becomes statistically attributable to anthropogenic climate change, defined as the first decade in which the Fraction of Attributable Risk is greater than 0.99 (FAR ≥ 0.99). Gray regions indicate grid cells where no DZD event attributable to anthropogenic climate change is projected to emerge before 2100. For regions with reservoirs, the ToFE is considered to be the first decade after the year of completion (Supplementary Fig. 6) of their respective reservoirs, when all DZD criteria are simultaneously met. By aligning the emergence timing with the operational onset of water storage infrastructure to reflect the real-world system resilience dynamics. The black stars denote the locations of the reservoirs threatened by DZD emergence. **b** Circular diagram illustrating the temporal distribution of ToFE by decades. The color scale indicates the percentages of grid cells (land areas) experiencing their ToFE distribution in each decade from 1900 to 2100. It provides a temporal overview of how the ToFE is distributed over time and the trends in DZD emergence.

The ToFE of DZD is influenced by the severity of the precipitation deficit and increases in evapotranspiration (SPEI48), river drought (SRFI48), and water demand (SWSI48), particularly in Africa (Supplementary Fig. 10). In parts of Asia and America, increased water consumption can influence the early emergence of DZD compared to other factors. This rise in water consumption is associated with population growth and socio-economic development, encompassing expanded water use across domestic, irrigation, industry, electricity, livestock, and mining sectors. These findings emphasize the importance of jointly considering all four drivers: climate, hydrological supply, event duration, and human demand, since no single factor can fully characterize a compound hydrological extreme event like DZD. Furthermore, the lower the thresholds applied to define the DZD, reflecting more severe and rare events, the later the ToFE will emerge, underscoring the complex relationship between event severity and its anthropogenic emergence (Supplementary Fig. 10). This compound approach highlights that water scarcity can be triggered by various drivers rather than a single stressor. For instance, a precipitation deficit without strong demand pressure may not induce water scarcity, while excessive demand alone may not trigger a water crisis if demand remains below supply. However, unsustainable consumption driven by population growth and socio-economic development alone can also trigger water scarcity if water use surpasses the available resource. Therefore, the simultaneous occurrence of these factors can lead to the emergence of an unprecedented acute water scarcity.

In addition, reservoir characteristics, specifically the Time for Reservoir to Dry (TRD), play a crucial role in detecting the ToFE of DZD. TRD serves as a proxy for how long a reservoir can sustain water supply under drought conditions when river inflow is the only source of water. The longer it takes for an unprecedented drought to drain water in reservoirs, the later the ToFE will occur, particularly in Mediterranean regions. An increase in TRD, quadrupling the TRD, will affect the ToFE of the 8% of the DZD-prone regions, causing later emergence than in Fig. 2a (Supplementary Fig. 11, Methods). Therefore, the duration of drier conditions, combined with rising human water consumption, can dry the reservoirs and trigger severe DZD, including reservoir-dependent regions. However, excluding both drought duration and TRD increases the event occurrence in both historical and future periods and raises their probability. This will delay the human-induced signal (FAR ≥ 0.99), leading to later ToFE compared to Fig. 2, particularly in the Mediterranean regions (Supplementary Fig. 12). In contrast, DZD emerges earlier in other regions because the probability of future events exceeds the pre-industrial baseline earlier, enabling earlier detection of FAR ≥ 0.99. Therefore, including the multi-year drought duration and TRD makes these events unprecedented versus pre-industrial conditions, highlighting their importance for understanding the emergence and magnitude of anthropogenic water scarcity and the critical role of reservoirs in water crisis vulnerability. These insights underline the need for future work research integrating dynamic reservoir operations and adaptive water management strategies where region-specific data is available.

Furthermore, the ToFE of unprecedented water stress and scarcity can be dependent on model structure and scenario pathways[38,39]. To address this, we use data from the CNRM model under two scenarios, SSP2-4.5 and SSP3-7.0. Both scenarios project that 51% of DZD-affected regions will face unprecedented water scarcity by 2100, with 22% experiencing emergence as early as 2020-2030 (Supplementary Fig. 21b, c). The influence of the scenario on DZD ToFE is region-specific (Supplementary Fig. 21b, c, f) due to the interaction between regional climate drivers and human water use. Both high (SSP3-7.0) and moderate (SSP2-4.5) scenarios can advance, delay, or have no change on DZD emergence, depending on the region. Model structure also drives spatial discrepancies (Supplementary Fig. 21a, b, d, e): CESM2-LE projects broader DZD regions in northern Africa, while CNRM highlights other regions such as South America and Australia. Nonetheless, both models consistently identify the Mediterranean, parts of southern Africa, and North America as key emerging hotspots.

Waiting time and duration of DZD

The recurrence and persistence of compound drought events are critical to understanding future water risk. In this context, we assess the waiting time directly by counting the number of months after the decade of the ToFE until the next event, for all consecutive DZD events until 2100, while the duration is calculated as the number of months a DZD event lasts. Both factors can importantly exacerbate the societal and ecological impact of DZD because its continuity is destructive and costly, especially when the waiting time is short and the duration is long. The duration plays a crucial role in determining the event's extremeness and affects the exposure and vulnerability of society. Short waiting times between successive events limit the recovery period, thereby amplifying stress on water systems.
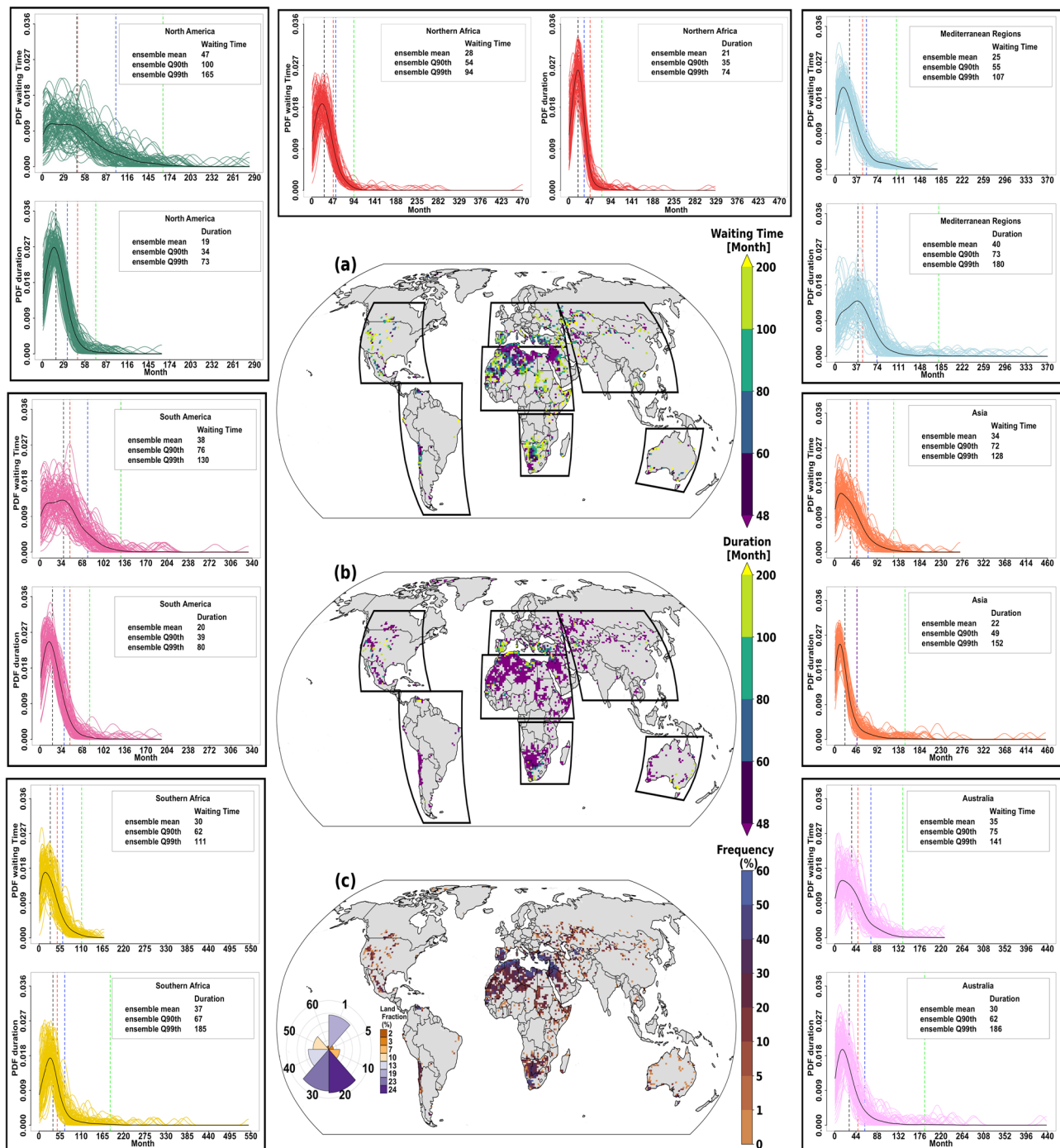
Fig. 3 | Characteristics of Day Zero Drought (DZD) events in terms of waiting time and duration, based on CESM2-LE simulations under the SSP3-7.0 scenario. The central spatial map shows the spatial distribution of the ensemble-mean waiting time (**a**) and duration (**b**) of DZD events, respectively, following the Time of First Emergence (ToFE) at each grid point of DZD-prone regions across the globe. **c** represents the spatial distribution of the frequency (%) of extreme DZD events, defined as those where the event duration exceeds the waiting time, indicating prolonged water scarcity impact and short recovery period. The accompanying inset circular diagram of **c** illustrates the distribution of these events, with the color scale indicating the proportion (percentages) of grid cells experiencing such conditions. This visualization highlights where and how frequently extreme DZD conditions with long duration and short waiting time emerge. The surrounding paired panels depict the Probability Density Function (PDF) of waiting time and duration for DZD events across seven DZD-prone regions. Colored lines represent the PDF of each ensemble of 100 CESM2-LE, while the black line is the ensemble mean of the respective PDF. The vertical dashed lines mark the ensemble mean (black), 90th percentile (blue), and 99th percentile (green) for each region. The red dashed line represents the monthly scale of the compound extreme event, which is 48 months. The period considered for each grid point started from the month after each decade of their respective ToFE and continued until 2100.

The spatial distribution and the Probability Density Functions (PDFs) of DZD duration and waiting time across hotspot regions reveal distinct regional variations in the magnitudes and the distribution (Fig. 3). The heavy-tailed PDFs, with the 99th percentile exceeding 48 months, suggest that climate change can cause long durations of DZD events, although such extremes remain rare events due to long waiting times between events. However, short waiting times and durations of less than 48 months are more likely to occur, as illustrated by the shape of their PDFs and their spatial distribution (Fig. 3a, b). Moreover, the probability of having a waiting time above 48 months

for all regions affected by DZD is above the 90th percentile. In terms of duration, the likelihood of an event lasting less than 48 months is above the 90th percentile, except for the Mediterranean Region, Southern Africa, Asia, and Australia, indicating shorter tails of waiting times and longer tails of duration. Thus, in these regions, the DZD tends to last longer with shorter waiting time periods. These prolonged DZD can dry up the reservoirs, heightening the risk of long-term acute water scarcity with a large-scale impact during the twenty-first century. This will be exacerbated by climate change in the future, cascading to "zero water" as many reservoirs will not have enough water to meet the demand of the projected population. Altered precipitation and river flow patterns can prolong the dry conditions and reduce the volume of inflows to freshwater systems, exacerbating water shortages. Increased evapotranspiration and water consumption deplete water sources (water available in rivers, lakes, and reservoirs) more quickly and prolong DZD duration. The volume of water that reservoirs can retain will decrease due to prolonged periods of stress caused by both climate change and human activities. As ecosystems are weakened and less capable of retaining water, even brief periods of rainfall may be insufficient to end a drought or replenish water supplies, limiting the recovery period before the next DZD event.

The duration distributions vary considerably in the tails compared to the waiting time, determining the likelihood of extreme DZD events with longer durations. The model agreement is high in simulating the waiting time and duration of the DZD. The 90th and 99th percentiles, the extreme upper tails, show some consistency among the ensembles, indicating that DZDs are projected to have a long-lasting duration but can also have long waiting times between events. An upper tail of the waiting time density greater than the duration denotes the possibility of rare DZD to occur in America and Northern Africa.

The localized nature of DZD characteristic is driven by the variation of climate (via SPEI48 and SRFI48), water consumption (via SWSI48), and reservoir capacity (via TRD) across regions, as the climate, the capacity of the reservoirs, agricultural irrigation, industrial development, and population-driven demand differ substantially across regions. To identify where DZD events will be most severe, Fig. 3c shows the DZD-prone regions and their frequency, defined as a case where DZD event duration exceeds its waiting time, indicating short recovery periods and prolonged impact. Almost 47% of the global high-risk regions will experience extreme DZD events with a frequency between 20% and 30%. Around 12% of the DZD-prone regions have a frequency of extreme prolonged DZD events above 50%, indicating that almost half of the events have longer durations than waiting times, suggesting frequent and severe water crisis conditions with substantial socio-economic impacts. Regions with high water demand and strained reservoirs, such as the Mediterranean, exhibit both high frequency and long durations of extreme DZD. In these areas, the compounded effects of hydro-climatic stress and human demands intensify the severity and persistence of DZD, exposing heightened vulnerability to water crises and limiting recovery capacity.

These findings underscore that the duration and waiting time of DZD are shaped by complex, location-specific socio-hydrological feedback. Moreover, the DZD characteristics are crucial for identifying vulnerable zones where adaptive water governance is urgently needed to mitigate future water crises. Understanding these localized dynamics enables more targeted drought preparedness and infrastructure resilience planning.

Impact of DZD on the population
We quantify the number of people living in each grid cell during the decade in which DZD first emerges (ToFE). We assess the population exposure across the total, rural, and urban populations. Results reveal a disproportionate exposure of vulnerable populations across time, regions, and warming levels (Fig. 4). Under the SSP3-7.0 scenario, over

753 million of the total population (Fig. 4a, almost 9% of the current global population) will be exposed to DZD, with populations in urban areas (467 million) more affected than in rural areas (286 million). The urban population is most exposed in the Mediterranean, with 196 million urban and 85 million rural residents at risk. In contrast, rural populations are disproportionately impacted in Northern Africa, Southern Africa, and Asia (Fig. 4d).

In rural areas reliant on rainfed agriculture and surface water, DZD will threaten livelihoods, food security through crop failures, and economic stability. Although urban areas generally benefit from more robust infrastructure, they remain highly vulnerable to DZD over the next few decades (Fig. 4c). As cities expand, rising water demand often exceeds supply, making the area susceptible to energy shortages, restricted domestic water consumption, and socio-economic instability.

DZD in terms of global warming levels
The Paris climate goals are expressed in terms of global warming levels (GWL), making it essential to assess the societal impact of DZD related to the warming level at the ToFE of DZD relative to the baseline period. By linking the ToFE of DZD-affected regions to their respective GWLs, we estimate the distribution of exposed populations. The results show that 61% of GWL related to the ToFE of DZD-affected regions are in the range of 1–2.5 °C (Fig. 4b). This indicates that over half of these regions will experience DZD in a 1–2.5 °C warmer world. Notably, more urban population would be exposed to DZD than rural population (Fig. 4e). The future impact on urban DZD-prone regions will be severe under these warming levels due to the higher population densities and escalating demand. Hitting the mark of 1.5 °C represents the maximum of the exposed population (Fig. 4e), with a total population of 488 million, which can be decomposed into 322 million of urban and 166 million of rural population, suggesting the urgent need to limit warming at most 1.5 °C. This study emphasizes how climate change, socio-economic development, and water scarcity interact to increase the DZD risks, particularly affecting vulnerable populations unequally, even before the most extreme warming scenarios are reached.

In addition, the risks of urban DZD are not just a future concern in a warming world, but also a near-term reality, with high population exposure by 2020 (Fig. 4c). These compounded challenges underscore the urgent need for proactive and targeted policy responses, particularly in regions where rapid development, insufficient water infrastructure, and climate vulnerability coexist.

Adaptation pathways and policy implications
The emergence of DZD highlights the urgent need for proactive, integrated water management within policy frameworks to address the compound risks of climate change and unsustainable water use. Climate policy and water security are tightly interconnected in the Sustainable Development Goals (SDGs)[53,54], so mitigation and adaptation strategies must align with global targets while fitting regional and community-specific needs for long-term resilience[55].

Defining DZD events as water scarcity driven by climate change underscores the challenges in sustainable water supply (SDG target 6.1) and efficient water use under stress (SDG target 6.4). Assessing the ToFE of DZD supports early warning signals (SDG target 13.1) and integration of climate adaptation strategies into water management policies (SDG target 13.2). Empowering communities to design local adaptation strategies fosters equitable and context-appropriate responses[56], through water conservation, crop selection, water storage solutions, and efficient cross-sectors water use, context-specific responses in DZD-prone regions.

Building resilience requires integrating local knowledge, adaptive cooperative management[57], water governance[58], and diversified supply strategies, including the re-planning of water reservoirs, desalination, rainwater harvesting, and wastewater recycling. Climate-resilient
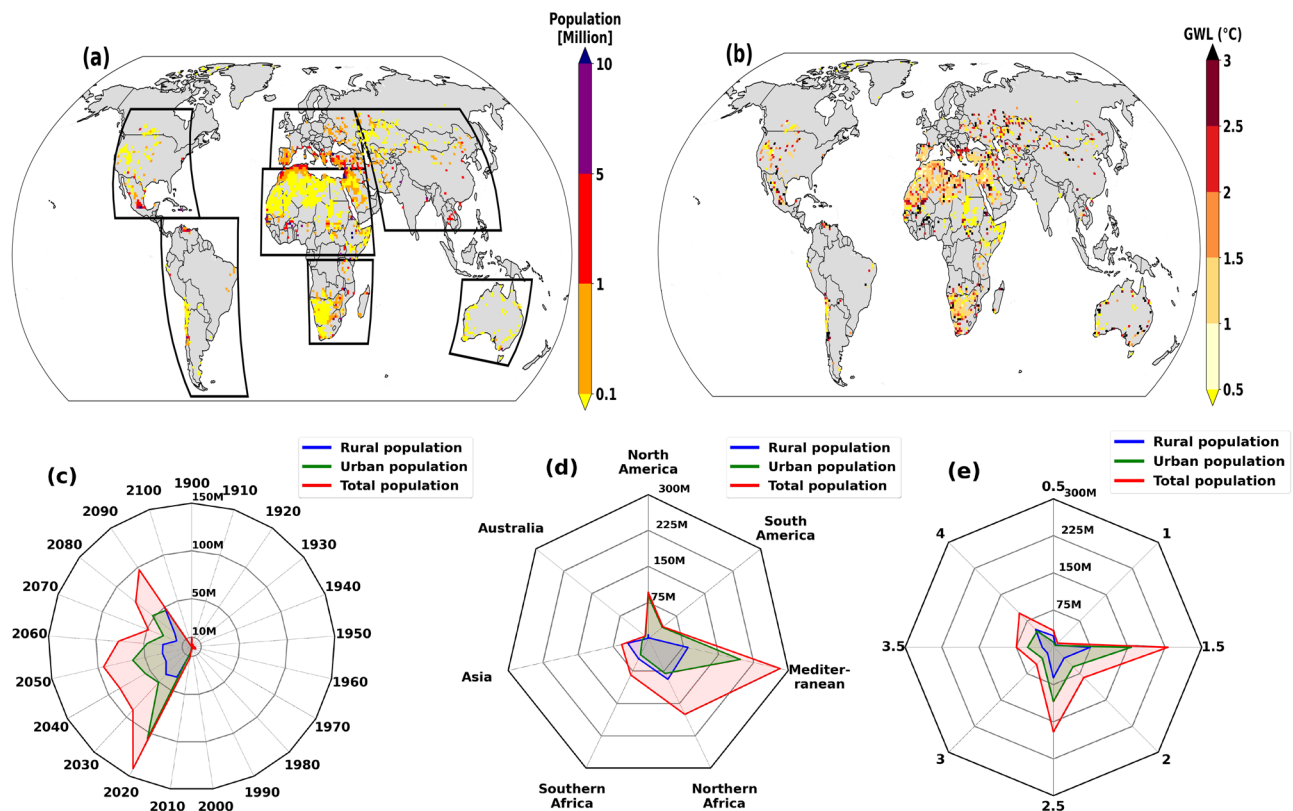
Fig. 4 | Population exposure and global warming levels associated with the Time of First Emergence (ToFE) of Day Zero Drought (DZD) based on CESM2-LE ensemble simulations under the SSP3-7.0 scenario. a Spatial distribution of the total population exposure at the ToFE of DZD across the global DZD-prone regions. The color scale indicates the total population (urban and rural) exposed when DZD first emerges in each grid cell. **b** Global distribution of the Global Warming Level (GWL, in °C above preindustrial) corresponding to the ToFE of DZD, providing insight into the warming levels associated with the onset of DZD events. **c** Circular diagram illustrating the rural, urban, and total population exposure to DZD at the ToFE, spanning the period from 1900 to 2100. **d** Regional distribution of rural, urban, and total populations affected by DZD, computed as the sum of exposed respective rural, urban, and total population within each regional hotspot (demarcated black box in **a**) at their respective ToFE. **e** Distribution of population exposure relative to the GWL at ToFE. Radar plots **c**–**e** emphasize the relative contributions of rural and urban populations to total exposure, highlighting disparities in vulnerability and exposure across both time and regions.

infrastructure investments, which have been underfinanced[59], need to balance conventional and innovative approaches to ensure sustainable water access in drought-prone regions.

Uncertainty in ToFE of DZD

A key limitation of this study is the reliance on the CESM2-LE and a limited number of CNRM simulations for the sensitivity analysis. CESM2-LE provides robust ensemble consistency, suitable for probabilistic analysis, but lacks scenario diversity and structural uncertainties across Earth System Models (ESMs). Conversely, the CNRM model includes more scenarios but has fewer ensemble members and lower spatial resolution, limiting its ability to capture localized extremes. These limitations underrepresent inter-model variability in drought drivers, including precipitation and evapotranspiration, whose trends may vary among ESMs[60,61], limiting our uncertainty assessment.

Moreover, CESM2-LE's land model assumes static aquifer storage, excluding dynamic groundwater variability. This overlooks the critical role of groundwater as a vital buffer during drought, particularly in groundwater-dependent regions. Groundwater contributes to the global water cycle, influencing river discharge and evapotranspiration, while also being altered by both climate change and human activities[62]. Incorporating dynamic groundwater processes is essential to improve water stress risks assessments. Groundwater is declining globally, leading to dry wells[63]. Climate change stresses groundwater[62] through increased use during droughts and reduced natural recharge, potentially worsening the impacts of continued drought[64]. Prolonged rainfall

deficits can disrupt the hydrological cycle in a warmer world and can lead to groundwater drought[65]. Despite its important role in water scarcity, global modeled and observed groundwater datasets remain scarce. However, its long-term relationship with atmospheric drought (partially captured by SPEI48; Supplementary Fig. 13) provides insight into its response to hydroclimatic stress.

Notwithstanding anthropogenic global warming, population growth and economics remain the major drivers of the water crisis by increasing demand[27,34]. Our study considers the socio-physical aspects of water security and excludes factors like national water policies, governance, quality, and environmental flow requirements.

The GRanD database provides valuable reservoir data but lacks information on real-time-varying hydrological dynamic details and includes unverified entries, limiting the number of reservoirs used. Although our study assumes stationary TRD, the static TRD effectively defines the minimum drought duration required to deplete reservoirs below critical storage levels, but it limits the ability to capture the future dynamic reservoir operations during drought. In the era of ongoing dam construction, time-varying TRD is essential for understanding how reservoir strategies influence water scarcity, but such data are currently unavailable. The interaction between socio-physical drivers and reservoir management is essential for defining compound climate extreme events[23,66] and assessing DZD impact. Despite data limitations, our approach provides a practical and reproducible framework for vulnerability assessment.

The reconstruction of historical total water consumption data (1850–2009) assumes smooth socio-economic transitions over time

and overlooks historical disruptions like wars, technological innovations, or abrupt policy changes. Moreover, the reliance on a scenario means that reconstructed trends reflect a world characterized by high socio-economic fragmentation and challenges to sustainable development, which may not fully align with actual historical pathways. These assumptions affect the accuracy of past water use estimates. Addressing these data gaps will help refine water scarcity risk analysis in the context of climate and socio-economic change.

Discussion

This study reveals when and where DZD may first emerge under climate change, emphasizing the importance of the compound drought duration and reservoirs[40] in driving the severity of long-term drought-driven water scarcity and the unprecedented nature of these events. Excluding these factors delays ToFE, particularly in reservoir-dependent regions (Supplementary Fig. 12). Integrating reservoir response and drought persistence dynamics into future models will improve the relevance and robustness of water scarcity for near- and long-term assessments while considering risk and mitigation benefits. Our findings align closely with Stolte et al.[67], highlighting the increase in the likelihood of urban drought in the future, a potential driver of urban DZD. In addition, it is important to consider the impact of upstream land use change, as it can intensify the effects of drought and exacerbate water scarcity in downstream areas[26].

Unlike broader water scarcity metrics like the Falkenmark indicator, used by Liu et al.[39], which use per capita water availability and relative population demand, our approach incorporates sector-specific water use and regional imbalance between supply and sectoral consumption (via SWSI) under human-induced climate. Note that SWSI on its own can identify water scarcity driven by high water consumption, but that can occur without climate-caused drought conditions. This distinction is important in the context of our study, as we define DZD as a prolonged anthropogenic drought-driven water scarcity caused by socio-physical factors, including water supply, human-made reservoirs, lakes, and sectoral water consumption. Therefore, it is essential to consider multiple indicators for assessing extreme events[68], including SPEI48, SRFI48, and SWSI48. Although this study focuses on socio-physical water scarcity, incorporating water quality and environmental flows, as highlighted by Liu et al.[9], is critical for a holistic understanding of future water risks.

Using the FAR method, we found that the contribution of human-induced climate change to DZD increases throughout the twenty-first century (Supplementary Fig. 9). Identifying ToFE with a very high attribution confidence (FAR ≥ 0.99) of human-induced signal relative to the pre-industrial period (1850–1899) provides robust scientific attribution, but it offers limited practical guidance for planning and adaptation, since most water infrastructure and management systems were designed based on the late twentieth-century (Supplementary Fig. 6) climatic conditions rather than pre-industrial norms. Regions with FAR < 0.99 (Supplementary Fig. 19) may still face DZD in the future, but with weaker anthropogenic attribution.

DZD, which has threatened Cape Town, is a multifaceted crisis that disproportionately affects low-income communities and exacerbates socio-economic inequalities[69]. It affects the domestic water supply, particularly in urban areas, with cascading effects on public health and societal risk. The impacts of drought vary across regions and sectors, with the least developed countries most vulnerable due to disparities in physical, social, economic, and knowledge-based factors[70]. In agriculture, DZD can reduce crop yields, threaten food security, and impact livestock through water and feed shortages. The need for sustainable irrigation of economically water-scarce cropland is critical to alleviating food insecurity[71]. Water-reliant industries and hydropower regions, including mining, can risk operational disruptions, energy shortages, and economic losses. Prolonged drought can degrade freshwater and terrestrial ecosystems, compromising water

quality, biodiversity, and long-term ecological resilience. These cross-sectoral impacts underscore the need for integrated potential solutions[29] and adaptation strategies with equitable water governance and management[58] at a regional scale. To support such efforts and reduce uncertainty in water scarcity assessment, expanded hydrological simulations across diverse models and emission scenarios are urgently needed.

Methods

Climate models simulations and observations

We use climate projection data from the Community Earth System Model version 2 Large Ensemble (CESM2-LE) simulation[72]. This is a 100-member single-model ensemble simulation using the Shared Socio-economic Pathways SSP3-7.0 scenario covering the period 1850 through 2100. The atmospheric data have a 1-degree spatial resolution, which serves as the reference for the interpolation of all CESM2-LE variables used in this study to ensure the consistency across datasets for the spatial analysis. We use monthly mean data, derived from daily data, including average temperature, maximum temperature, minimum temperature, and total precipitation from CESM2-LE. We also use river discharge (Supplementary Fig. 2) over land from the Model for Scale Adaptive River Transport (MOSART), the CESM2-LE river model component. In addition, we use the same variables from the European Centre for Medium-Range Weather Forecasts (ECMWF) Reanalysis v5 (ERA5-Land) within the period 1979–2022, as well as river discharge data from the Global Flood Awareness System (GloFAS) hydrological time series forced with ERA5 meteorological reanalysis (GloFAS-ERA5). To assess the sensitivity of our results to model structure and emission scenarios, we also include simulations from the Centre National de Recherches Météorologiques (CNRM) model under both SSP3-7.0 and SSP2-4.5 scenarios. For consistency, we analyze 10 ensemble members available for each scenario and consider the same hydroclimatic variables as used with CESM2-LE. Due to the coarser spatial resolution and limited ensemble size of the CNRM simulations relative to CESM2-LE, the CNRM model is used exclusively for sensitivity analysis of the event emergence time. The CESM2-LE large ensemble enables us to compute probabilistic estimates of the ToFE, duration, and waiting time of extreme events. Our 100-member CESM2 large ensemble provides enough data to robustly estimate extreme event statistics. Only CESM2-LE and CNRM provide the variables necessary for our analysis, so other large ensemble simulations cannot be used in our study.

We use the global reservoirs database, which includes information on reservoir location, capacity, and the long-term average discharge (1971–2000) available from the Global Reservoir and Dams (GRanD)[73] database. The global reservoir database includes both reservoirs constructed by humans and natural lakes, according to Lehner et al.[73]. The GRanD database version 1.3 was used due to its highly adaptable geodatabase that offers expanded attribute coverage and spatial precision, making it possible to implement regional or global analysis at unprecedented spatial resolution[73–75]. We assigned reservoirs to the closest grid point in CESM2-LE to facilitate integration with climate model outputs.

The monthly global gridded water consumption data for sectoral water use under SSP3 and SSP2, and the Representative Concentration Pathways scenario, RCP6.0 and RCP4.5, covering the period from 2010 to 2100, were downloaded from Khan et al.[76]. Both scenarios are available from the same five Global Climate Models (GCMs): GFDL, HADGEM, IPSL, MIROC, and NORESM. We use the available SSP3-RCP6.0 data due to the unavailability of sectoral water use data for SSP3-RCP7.0. We consider the available water demand data from different sectors, such as domestic, irrigation, industry, electricity, livestock, and mining, to capture the socio-economic development water use demand. To our knowledge, there are no global historical and observed data for sectoral water consumption, covering in particular domestic, irrigation, industry, electricity, livestock, and mining, for the

historical period from 1850 to 2009. This lack of historical and observational data represents a major challenge for the analysis of long-term water demand. Therefore, we reconstruct the water consumption data from 1850 to 2009 using a backward nonlinear logarithmic regression approach based on the Dose-Response Curve (DRC) model in R[77]. The model is trained with each specific month of future water consumption for the period 2010–2100 and then applied to predict past values. Specifically, the logarithmic curve DRC.logCurve() function is used to estimate water consumption for each month of the year for the period 1850–2009. This approach is implemented for each grid point from the global climate models provided by Khan et al.[76] to obtain a monthly gridded long-time series of water demand for the study period, from 1850 to 2100, for each grid. Importantly, to preserve the seasonal cycle and interannual variability, the nonlinear model was fitted independently for each month: for example, the curve was fitted using all January values from 2010–2100 to reconstruct the backward trend for January from 2009 to 1850; this process was repeated separately for each calendar month (January to December), in each grid cell of each GCMs. This method allows us to generate plausible historical estimates that align with the socio-economic trends incorporated in the scenario data, while recognizing the associated uncertainties. We acknowledge that this method introduces uncertainties as it assumes smooth socio-economic transitions over time and does not explicitly account for unexpected historical disruptions in water use patterns or development pathways, such as technological innovations or abrupt policy changes. Additionally, the reliance on the scenario means that reconstructed trends reflect a world characterized by high socio-economic fragmentation and challenges to sustainable development, which may not fully align with actual historical pathways. Despite these limitations, this reconstruction approach offers an estimate of historical water consumption trends, maintaining spatial, temporal, and sectoral variability. The spatial patterns and temporal evolution of water demand, along with inter-period differences, are illustrated in Supplementary Fig. 3. These reconstructed datasets serve as structured estimates to support consistent analysis across regions and sectors. The spatial resolution of all data is interpolated to the CESM2-LE and CNRM resolution using the first-order conservative remapping (remapcon) method from the Climate Data Operator[78] (CDO) for their respective analysis.

We also use global spatial population datasets from the history database of the global environment (HYDE), version HYDE3.3 from Klein Goldewijk et al.[79], to assess the population exposure from 1900 to 2009 at decadal intervals. In addition to that, we use the global spatial population projections SSP3 scenario obtained from the National Center for Atmospheric Research (NCAR)[80], from 2010 to 2100, at decadal intervals to assess the future population exposure. The population datasets were interpolated to a 1-degree spatial resolution for our study, the same grid as CESM2-LE, using the sum of the source points remapping (remapsum) method from the CDO to conserve the total sum of the population.

Water stress indices

The drought index, Standardized Precipitation-Evapotranspiration Index (SPEI), is a widely used indicator for investigating drought characteristics[81–86], including onset, duration, and magnitude. This study uses the SPEI to quantify and classify drought severity due to its capacity to reflect the change in water deficiency. The index does not account for actual water losses from the land surface but considers potential evapotranspiration (PET), a significant factor[87] in the future risk of extreme drought[83], making it more robust in categorizing drought and detecting its onset and evolution in the context of global warming[88] due to its contribution to the interaction of land-atmosphere conditions and drought[87]. Thus, the monthly gridded SPEI was obtained through the method proposed

by Vicente-Serrano et al.[88] using the modified Hargreaves method[89] to investigate the importance of the range of maximum and minimum temperatures in drought conditions. Moreover, the SPEI allows comparisons between regions across different climatic conditions and considers the onset and duration of drought. The SPEI can be used to investigate the impact of prolonged multi-year drought trends on hydrological and ecological variables, as well as on water storage deficits[90,91]. SPEI can effectively be utilized to depict the hydrological drought on a longer time scale[91]. However, hydrological drought is a complex phenomenon involving various factors[92–94] such as runoff or stream flow[95], water balance, human activities, and water demand. The interaction between precipitation, soil moisture, runoff, recharge, groundwater, and discharge has been known[65], but its application to drought is relatively recent. Thus, the causes of hydrological drought are complicated as they involve the atmosphere and hydrological processes that supply moisture to the atmosphere, contribute to water storage, and generate runoff to streams[93]. In addition, the streamflow drought will be defined as a multi-year insufficient river discharge, as most of the water supply comes in the form of river flow or runoff after all surface physical processes have been completed. In snow-fed river systems, river flow can still act as a water supply independent of immediate precipitation inputs. For instance, during periods of low precipitation, melting snow can sustain river flow. This is where the Standardized River Flow Index (SRFI) plays a crucial role, as it captures river drought conditions based on streamflow variations, reflecting both precipitation-driven and non-precipitation-driven water inputs. Therefore, we use a single input standardized drought index, called SRFI, the same as Vicente-Serrano et al.[96], to represent and categorize the severity of the river flow resource depletion. The river discharge data was used as the input to calculate SRFI. The concept of the calculation of SPEI and SRFI is made by fitting an empirical cumulative distribution function to reference periods (1979–2014), using the spei() function in R as proposed by Begueria and Vicente-Serrano[97]. The fitted distribution is then applied to the monthly cumulative precipitation-evapotranspiration (SPEI) or streamflow (SRFI) to obtain cumulative probabilities, which are transformed into a standard normal distribution. This process effectively standardizes the data relative to the reference period (1979–2014), allowing for easy interpretation. Both drought indices, SPEI and SRFI, were computed at a 48-month timescale for each grid cell in every ensemble member of CESM2-LE and CNRM, covering the period from 1850 to 2100.

To investigate the degree of water scarcity, we adopt the Standardized Water Scarcity Index (SWSI), which is conceptually equivalent to the Supply and Demand Balance Index introduced by Huang and Yin[98], to represent the overexploitation of the water resources when the demand exceeds the supply. This index captures the imbalance between water availability and demand by taking the ratio of total water supply to total water consumption. The SWSI with a time scale of 48 months is used. The SWSI was chosen due to its capacity to represent the dynamic processes[98] between the interaction of the water supply and demand for domestic usage and production in a region. The SWSI48 is the ratio of the 48-month accumulated total water supply and 48-month accumulated total water demand. The total water supply is estimated as the sum of surface water resources, including river flow and the net water balance (precipitation minus evapotranspiration), representing the available freshwater availability. The total water demand is the sum of water consumption from all sectors, such as domestic (dom), irrigation (irrig), industry (ind), electricity (elec), livestock (liv), and mining (min). Therefore, to calculate SWSI48, the total water consumption from the five Global Climate Models (GCMs) provided by Khan et al.[76] (GFDL, HADGEM, IPSL, MIROC, and NOR-ESM) is randomly distributed across the total water supply from the

CESM2-LE and CNRM (see Supplementary Fig. 1 for further details).

$$SWSI48 = \frac{TWS_{48}}{TWC_{48}} = \frac{(Prec - E + flow)_{48}}{(dom + irrig + ind + elec + liv + \min)_{48}} \quad (1)$$

where TWS is the total water supply, $Prec$ represents the precipitation, E is for evapotranspiration, $flow$ for the river flow, and TWC represents the total water consumption.

The definition of water scarcity from Huang and Yin[98] is used for the degree of SWSI48, as extreme lack of water [0,0.3], acute shortage of water [0.3,0.6], moderate water shortage [0.6,0.9], slight shortage of water [0.9,1], and no shortage of water [≥1].

To assess the interdependence among the water stress indicators used in this study, we computed spatial correlations between the ensemble means of the SPEI48, SRFI48, and SWSI48 derived from CESM2-LE simulations over the period 1850–2100. All-time series were detrended to remove systematic long-term trends associated with climate change and ensure that correlations reflect interdependence among the indicators. Supplementary Fig. 4 shows strong positive correlations across most regions, indicating that the water stress tends to vary together over the multi-year time scales of 48 months. In contrast, the negative correlations between SPEI48 and SWSI48, and between SRFI48 and SWSI48, are generally weak, particularly across Africa, reflecting the influence of non-climatic drivers such as water demand on SWSI48. Overall, both weak positive and negative correlations are observed in many regions, suggesting a more complex relationship between climate-driven drought indicators (SPEI48 and SWSI48, and SRFI48 and SWSI48).

Bias correction (BC)

In order to minimize the model errors, this study used a bias correction method to reduce model bias. Supplementary Fig. 1 shows a more detailed structure of the steps in the methods and the processes used in this study. The monthly database from ERA5-Land (1979–2022) was used to calculate ERA5's SPEI48 and SRFI48, with 1979–2014 as the reference period, which is used as the observational drought indices reference to calibrate the drought indices for each ensemble member of CESM2-LE individually. Although observational sources are the best to achieve the ideal bias correction, we opted for reanalysis products because they consistently assimilate a variety of variables in a physically consistent manner, and it is assumed to be close to observed data. This choice ensures global coverage and temporal completeness, particularly important in data-sparse regions or for long historical records where high-quality observational data are unavailable or inconsistent. The ERA5-Land dataset was found to be a trustworthy reference to calibrate CESM2-LE indices. In order to increase our confidence in future extreme drought projections, we applied the univariate Quantile Delta Mapping (QDM), as Ansari et al.[99] found it to be more robust for the correction of indices. Supplementary Fig. 14 shows that direct correction (post-processing QDM) of the drought indices as a single variable reduces the bias between ERA's SPEI48 and the ensemble mean of the CESM2-LE's SPEI48 and manages to capture the distribution of SPEI48. In addition, Van de Velde et al.[100] stated that the simpler univariate BC methods are better to use for climate change impact assessment, as the multivariate BC methods failed to handle non-stationary climate conditions. This approach maintains the model-projected climate change signal while simultaneously correcting the distributional biases. The QDM bias correction method, introduced by Cannon et al.[101], is a cumulative distribution function (CDF)-based bias correction method designed specifically to reduce the biases between the modeled and observed distribution of drought indices, while preserving the model-projected climate change signal. The additive form of QDM is applied to bias correct the systematic biases in each quantile of the drought indices calculated from the CESM2-LE and CNRM simulations, using the ERA-derived indices as observational

references while preserving the model-projected absolute changes across all quantiles of the distribution. The important concept of QDM is its ability to maintain the trend in all the quantiles within the distribution of the climate model output, which is important when future changes are not uniform across the distribution. It is used to quantile detrend the model projections and adjust distributional biases in model projections, ensuring the sensitivity of the underlying climate model without affecting the distribution[101–103]. The QDM begins by identifying the corresponding quantiles of the observed, model historical (or reference for the calibration), and the model future projection, as a corresponding quantile-based correction derived from the model-observation mapping. Instead of directly fitting the full distribution of the future model, QDM quantifies the change at each quantile between the historical and future period model values at that same quantile level. These changes are then applied to the observed value at the corresponding quantile, retrieved using the inverse CDF of the observed data. This allows distribution biases to be corrected while maintaining quantile-specific climate change signals, thus preserving the sensitivity of the climate model. The univariate bias correction was performed using the QDM method available in the Multivariate Bias Correction (MBC) package in R. For each grid cell, drought indices from each member of the CESM-LE and CNRM are corrected independently, using their quantile location relative to the observed (ERA5) drought indices. Specifically, each value of SPEI48 and SRFI48, computed from each grid cell of every ensemble member of the CESM2-LE and CNRM datasets, within the period 1850-2100, is corrected as a single variable following the direct QDM approach, respectively. To correct the bias in SWSI48, we applied the univariate QDM method to the total water supply (precipitation-evapotranspiration + river discharge) at each grid cell of each ensemble member of CESM2-LE and CNRM, treated as a single aggregated time series rather than bias-correcting each individual component (i.e., precipitation, evapotranspiration, and river discharge). This aggregated variable represents the net variable water and is more relevant for capturing water scarcity as reflected in SWSI48. We could not apply the bias correction of the total water demand (consumption) due to the unavailability of consistent observed sectoral water use data across the historical period at the global scale.

To assess the effect of different bias correction strategies, we evaluated both pre- and post-processing approaches using CESM2-LE under the SSP3-7.0 scenario. As shown in the Supplementary Fig. 14, post-processing (i.e., direct bias correction of SPEI, Supplementary Fig. 14c) better captures the distribution of SPEI from ERA5 (Supplementary Fig. 14a), while pre-processing (i.e., bias correction of precipitation and temperatures prior to computing the index; Supplementary Fig. 14d) tends to introduce additional bias, particularly by amplifying wet conditions. These results support the effectiveness of the post-processing approach in preserving the observed statistical properties of the drought indices.

Furthermore, we evaluated the distributional properties of the corrected indices using Q-Q plots, shown in Supplementary Fig. 14e–j. These plots compared the quantiles of SPEI48 from CESM2-LE (with and without correction) and ERA5, both at the global mean scale and for a representative grid point (longitude 43.40° and latitude −23.21°). The Q-Q plot revealed that the bias-corrected indices closely follow the normal distribution, especially compared to the raw model output. At the grid level (longitude 43.40° and latitude −23.21°), the correction successfully adjusted for extreme droughts and ensured consistency with observed drought characteristics.

Overall, our bias correction method effectively improves the distributional agreement between CESM2-LE and ERA5, while maintaining long-term trends. This provides a more accurate basis for assessing drought characteristics and their implications for water scarcity under historical and future climate conditions. As with most bias correction methods, QDM has limitations, as it assumes that model biases are

relative to the present reference dataset, which may change in the future. Although this assumption simplifies the correction process, it may not hold under evolving climate conditions.

Time for Reservoirs to Dry (TRD)

An important aspect of drought impacts is the availability of water in reservoirs. The onset of drought conditions and continuing water demand will also affect reservoir water levels. To assess the severity of the drought events, we have to also consider the Time for the Reservoir to Dry (TRD) as the ratio of the maximum capacity and the monthly average discharge at reservoir locations, by considering only the reservoirs with verified, good and fair quality index[73], which represents 93% of the GRanD' reservoirs (Supplementary Fig. 5).

$$TRD = \frac{maximum\ capacity\ of\ the\ reservoir}{monthly\ average\ discharge\ at\ reservoirs} \qquad (2)$$

For human-made reservoirs, the maximum capacity refers to the maximum value of the storage capacity, and for natural lakes, it is the given lake level by Lehner et al.[73]. The lack of water level time series in the reservoirs makes it hard to estimate the time scales by which they might run dry. Instead of the available capacity of the reservoir (maximum minus minimum capacity), the maximum capacity was used because it was a readily available parameter for most reservoirs and due to the lack of the points layer of minimum capacity in the GRanD database. Moreover, climate change may alter the future operation of reservoirs, so using the maximum capacity is useful for assessing the suitability of water storage strategies. The TRD is similar to the resident time (time of water spent in reservoirs) and can be considered as the duration to take for a drought event to dry the water in the reservoirs if the only source of the water supply of the reservoirs is the depleted river flow during a drought period. This reflects hydrological drought situations in which rivers continue to flow, albeit at diminished levels insufficient to meet water demand, allowing assessment of how long reservoirs can sustain supply under such stress.

Compound multi-year hydrological drought

We define the compound multi-year drought, based on the IPCC[104] definition of a compound event, as extended periods, often spanning several years (e.g., 48 months or 4 years for this study), during which multiple hydrological indicators, such as long-term rainfall deficiency, streamflow, water demand, and reservoir storage, experience simultaneous and persistent deficits. Here, these droughts are characterized by the concurrent occurrence of below-normal water availability across various hydrological systems, exacerbated by interrelated factors such as reduced precipitation with increased evapotranspiration (SPEI48), increase in water consumption (SWSI48), and depleted river flow (SRFI48). The compound nature of these events indicates the presence of multiple interacting drivers that collectively intensify water scarcity over a prolonged period.

Day zero drought definition

We define "Day zero drought" (DZD) as an acute water scarcity event driven by a compound multi-year hydrological drought, during which water demand exceeds water supply under prolonged drought conditions. DZD occurs due to a critical imbalance between supply and demand, driven both by climate-induced reduction in supply and anthropogenic pressures increasing demand.

In fact, water can be retained in the reservoir through different parts of the hydrological cycle and different resident times (time of water spent in reservoirs) considered similar to TRD. As the river flow contributes to the long-term storage of water in the reservoir, we considered the river discharge to be an appropriate parameter. DZD is the impact of the simultaneous occurrence of a long-term (48-month)

critical rainfall deficiency and extreme dearth of water of low-flow river discharge during a prolonged drought in the context of global warming and long duration exceeding the time for the reservoirs to run out of water. This is formalized as follows:

$$DZD\ occurs\ if$$
$$\begin{cases} SPEI48 - 1.5 \cap SRFI48 - 1.5 \cap SWSI480.6,\ dur_{ce}\ TRD,\ if\ reservoir\ exists. \\ SPEI48 - 1.5 \cap SRFI48 - 1.5 \cap SWSI480.6,\ if\ there\ is\ no\ reservoir. \end{cases} \quad (3)$$

where dur_{ce} is the duration of the compound extreme. The identification of DZD was carried out at each grid cell across each of the 100 members of the CESM2-LE model, offering a comprehensive and probabilistic perspective on future water scarcity risk.

However, global warming is expected to disrupt and intensify the variability of the water cycle[16], leading to increasingly frequent and severe fluctuations between excessively wet and dry periods[17]. Warmer climates are projected to enhance the evapotranspiration, resulting in dry conditions[18]. Additionally, reductions in precipitation and surface runoff are expected in many regions[16], further increasing the likelihood of both climatological and hydrological droughts[19–22]. Moreover, population growth, economic development, and expansion of modern agriculture drive the rise in water consumption, placing additional pressure on water resources. Therefore, dry conditions driven by anthropogenic climate change and socio-economic development are jointly altering the global balance between water supply and demand, thereby amplifying the risk of DZD. Our concept distinguishes between drought and water scarcity, while also capturing their interaction in driving the DZD event. Drought refers to a reduction in water availability either through decreased precipitation, increased evaporation, or reduced river flow. In contrast, water scarcity arises when water demand exceeds the available water supply. Water Scarcity is often human-driven from anthropogenic pressure, such as population, growth, agricultural expansion, industrial use, and mismanagement of water resources. Water scarcity can occur even in the absence of climate change if water use is unsustainable. In this study, we focused on water scarcity driven by drought, where the reduction of water supply is driven by dry conditions. In this context, the water stress is considered as a result of a compound event due to atmospheric conditions (precipitation and evaporative demand; SPEI48), streamflow conditions (SRFI48), and demand condition (SWSI48) of 48-months occur with important depletion of water supply and increase of water demand; and where the duration of the event is longer than the time of the closest reservoirs to dry (TRD). This study offers a global-scale assessment of DZD emergence and its characteristics, capturing the interactions between climate human-driven factors.

Therefore, DZD is considered as an extreme water scarcity event, characterized by the fact that the water resources available in a region are largely below the limited reservoir's capacity compared to the pre-industrial period. This is attributed to both anthropogenic climate change and an increase in water use. To our knowledge, this study is the first global-scale assessment of the timing of the emergence of Day Zero Drought conditions and its characteristics. DZD is characterized by the concurrent exceedance of critical threshold in four indicators: (1) The standardized Precipitation-Evapotranspiration Index (SPEI48) below minus 1.5 (SPEI48 ≤−1.5, exceedance of 1.5 standard deviations, signifying 1.5 standard deviation droughts to classify the arid atmospheric condition, through prolonged deficits in precipitation and increased evapotranspiration, leading to a long-term surface water stress and can significantly influence the change in groundwater (Supplementary Fig. 13). (2) The Standardized River Flow Index (SRFI48) below minus 1.5 (SRFI48 ≤−1.5, exceedance of 1.5 standard deviation), signifying 1.5 standard deviation droughts, to detect the depletion of river flow conditions, representing the state of the severe drought in river flow during dry periods. (3) The Standardized Water Scarcity Index (SWSI48) below 0.6 (SWSI48 ≤0.6) is used to quantify

the imbalance between total water supply and demand and to represent the long-term average insufficiency of resources relative to demand during periods of drought, leading to an acute water scarcity. (4) The duration of the compound event (dur_{ce}) exceeding the estimated time for reservoir depletion (TRD), when reservoirs exist. If no reservoir is present, the DZD is defined by the first three indicators. This framework reflects the reality that water scarcity emerges from the convergence of multiple stressors. Each indicator plays a distinct but interrelated role in defining DZD; therefore, none is weighted as more important than another. Their simultaneous exceedance is necessary to identify a DZD event, filtering out less severe or isolated events. For instance, precipitation deficits alone may not result in a crisis without demand pressure. i.e., in low low-demand case, just as high demand may not lead to scarcity if the supply is still enough. Similarly, even in the absence of climate variability, unsustainable consumption alone can trigger water scarcity if water use surpasses the available resource.

To evaluate the CESM2-LE ability to reproduce observed compound drought conditions, we compared the spatial distribution of compound hydrological extremes computed from the ERA5-Land reanalysis and CESM2-LE (ensemble mean of the number of compound hydrological events) data for the period 1979–2022. Specifically, we examined the number of occurrences where both 48-month scales of Standardized Precipitation-Evapotranspiration (SPEI48) and Standardized River Flow Index (SRFI48) were less than or equal to −1.5. This threshold represents severe to extreme dry conditions. Instead of comparing the ToFE of compound events, we investigate the number of events of joint occurrences with $SPEI48 - 1.5 \cap SRFI48 - 1.5$. Due to the lack of observed data on total water consumption across all sectors (domestic, irrigation, industrial, electricity generation, livestock, and mining), we were unable to include the 48-month Standardized Water Scarcity Index (SWSI48) in this observation comparison. The result (Supplementary Fig. 18) indicates that CESM-LE reasonably captures the spatial patterns of compound events defined by $SPEI48 - 1.5 \cap SRFI48 - 1.5$, as observed in ERA5. Although ERA5 exhibits slightly more compound events overall, the CESM2-LE ensemble mean estimates comparably and even exceeds ERA5 over China and Russia, indicating possible regional differences in model response.

Detection of the time of first emergence

In this study, we use the Fraction of Attributable Risk (FAR) of the joint probability to define the Time of the First Emergence (ToFE) of the DZD. FAR has been found to be effective in identifying the anthropogenic signal behind extreme events[105–107] such as DZD. According to Perkins-Kirkpatrick et al.[105], FAR can be useful for understanding climate change signals, but more useful results are achieved by refocusing attribution questions on changes in impact return value and magnitude across large samples. To the best of our knowledge, the evaluation of ToFE of the DZD relative to the anthropogenic signal with a predefined threshold of joint probability by FAR has not yet been carried out. Therefore, this study proposes an innovative method to assess the ToFE of compound extreme events by considering human-induced attribution. Few studies have used different alternatives to define or identify the ToFE when the hydrological drought differs from their past counterparts[38]. We are aware that even with such different methods, including our method here, uncertainties may arise, for example, due to internal variability[108] or the considered scenarios[109]. By applying the FAR method, we measure the influence of anthropogenic climate change by comparing the probability of occurrence of DZD in the baseline period (pre-industrial period: 1850–1899) with the anthropogenic forcing period. We identify DZD events using a threshold-based approach, as outlined in Eq. (3). This ensures that the events are derived from the indices (SPEI48, SRFI48, and SWSI48) and reflect extreme drought event conditions and acute water scarcity. By

applying a threshold-based approach, we transform the continuous drought indices into distinct, binary events (e.g., DZD or no DZD). Which aligns with the requirements for FAR analysis. Once the DZD events are identified, the events are treated as independent occurrences, ensuring that the FAR method is aligned with its intended purpose of analyzing distinct extreme events. The calculation of the probability of the forcing events has been conducted on decadal time scales. The FAR is based on the change in the occurrence of an independent event, which is quantified by dividing the probability of independent DZD events in the future by the preindustrial condition.

$$FAR(t) = 1 - \frac{P_{preindustrial}}{P_{forcing}(t)} \ with \begin{cases} P_{preindustrial} = \frac{\sum_{ens1}^{ens100} event_{i,preindustrial}(DZD)}{N_{preindustrial}} \\ P_{forcing}(t) = \frac{\sum_{ens1}^{ens100} event(t)_{i,forcing}(DZD)}{N_{forcing}(t)} \end{cases}$$

(4)

Where $P_{preindustrial}$ represents the probability of the counterfactual scenario, which is calculated as the ratio between the total number of DZD event occurrences across all 100 ensemble members during the preindustrial period (1850–1899) and the total number of samples within the same period ($N_{preindustrial}$). While $P_{forcing}(t)$ represents the probability under the factual scenario, which is the ratio between the decadal total number of DZD event occurrences across all 100 ensembles during each decade from 1900 to 2100 and the total number of samples during that decade ($N_{forcing}(t)$). The ToFE of DZD is identified as the first decade in which the FAR is greater than 0.99, where a 99% probability of the impact of the acute water scarcity that has emerged can be associated with a human-induced signal after the decade of completion of reservoirs (Supplementary Fig. 6). We computed the ToFE by considering the year of construction of a reservoir. Each reservoir has a different year of construction; therefore, if a reservoir existed in the considered grid point, the DZD detection period would extend from the year of completion to 2100. But if there is no reservoir, we use 1900–2100. Hence, we aim to detect events that have not occurred during the preindustrial period, but which will occur and intensify in the future as a result of anthropogenic global warming. In that sense, we identify unprecedented hydrological extreme events.

DZD characteristics: waiting time and duration

While the ToFE is an important measure of global warming impacts, its true impact is measured by how long these events last and how soon they will re-occur once they have emerged for the first time. The length of time of a DZD event is defined as the DZD duration, while the waiting time is identified as the time elapsed between the end of the previous event and the start of the next consecutive DZD event, as illustrated in Supplementary Fig. 8. To quantify these characteristics, we calculate the DZD duration and waiting time at each grid cell globally across the CESM2-LE for all ensemble members. We calculate the waiting time directly by counting the number of months after the decade of the ToFE under anthropogenic influence until the next event, for all consecutive DZD events until 2100, while the duration is calculated by the length of a DZD event once it occurs.

In addition, we assess the frequency of extreme DZD conditions, characterized by events that are both frequent and prolonged. Specifically, for each grid point and each ensemble member of CESM2-LE, we identify all DZD events occurring between the decade of ToFE and the year 2100. We then count the number of DZD event where its duration exceeds the waiting time, i.e., cases where the DZD event persists longer than the recovery period before the next event. These counts are aggregated at each grid across all 100 members of CESM2-LE within the ToFE and 2100. The frequency of extreme DZD conditions is computed at each grid cell as the ratio of the sum of these events to the total DZD events across all members of CESM2-LE within

the ToFE and 2100 period. This spatially explicit frequency is then mapped globally (Fig. 3c) to highlight regions most vulnerable to sustained and recurrent DZD conditions.

For each DZD-prone region shown in central spatial map of Fig. 3, we then average the values across all grids located within the regions. To characterize the statistical distribution of these metrics, we fit probability density functions (PDFs) to the distributions of DZD duration and waiting time.

Global warming level (GWL)

The ToFE depends partly on the used global warming scenario. In order to provide an alternative view, we also estimated the global warming levels at each DZD event emergence. We use the method proposed by Batibeniz et al.[110] to calculate the GWL, but for this study, we consider the difference between the global 30-year climatology backward on the analyzed decade (1900–2100) and the global mean temperature of the pre-industrial period (1850–1899). The GWL is the value of the GWL in the decade of ToFE.

Sensitivity analysis

We tested the sensitivity of ToFE to six factors. Firstly, the threshold for defining the multi-year compound drought can influence the detection of DZD. Therefore, to test the robustness of the DZD definition, we performed a sensitivity analysis using different thresholds for SPEI48, SRFI48, and SWSI48 (Supplementary Fig. 10). First, we modified the SPEI48 threshold to be below −2 and kept SRFI48 below −1.5 and SWSI48 below 0.6 (Supplementary Fig. 10a, i). The ToFE emerges later than in Fig. 2a, particularly in Africa, where ToFE is sensitive to SPEI48, i.e., to the decreasing precipitation and increasing evapotranspiration. Next, we slightly changed SRFI48 to be below −1.6, SPEI48 to be below −2, and kept SWSI48 below 0.6 (Supplementary Fig. 10b, j). The ToFE remains almost the same, and the ToFE emerges later by increasing the severity of SRFI48 to be below −2 (Supplementary Fig. 10c, k), particularly in the northern part of Africa. Then, as we continued to modify SRFI48 so that it is less than −1 (Supplementary Fig. 10d, l), the ToFE becomes earlier than Fig. 2a, mostly in the northern part of Africa. The ToFE is sensitive to the severity of the streamflow drought in Africa. After that, we repeated the same analysis, but considering SWSI48 less than 1, SPEI48 less than −2, and SRFI48 below −1.5 (Supplementary Fig. 10e, m); while SRFI48 below 1.6 for Supplementary Fig. 10f, n. The results show that ToFE is more likely to start earlier than Fig. 2a in a few regions, meaning that ToFE is more likely to be sensitive to streamflow depletion (SRFI48) and increased water consumption (SWSI48). In the latter case, we kept SPEI48 below −1.5 and SRFI48 below −2 with SWSI48 below 1 for Supplementary Fig. 10g, o; and SWSI48 below 0.6 for Supplementary Fig. 10h, p. The results show the sensitivity of the ToFE to SRFI48 and SWSI48; thus, the ToFE emerges later than Fig. 2a in Africa but earlier in other regions. Therefore, we can conclude that the ToFE of DZD is more sensitive to the severity of decreasing precipitation and increasing evapotranspiration (SPEI48), the river flow drought (SRFI48) and increasing water demand (SWSI48), particularly in Africa, while increasing water consumption solely have an impact on the early emergence of ToFE in some parts of Asia and America, compared to the other factor. The SRFI48 and SWSI48 are more closely related to the actual availability of river flow and water use, respectively. When water demand rises, the available water supply (e.g., river flow, even if unaffected by precipitation) becomes insufficient to meet demand, triggering drought-like conditions (or water scarcity) in terms of availability.

Secondly, to assess whether the treatment of grid cells with and without (as defined in Eq. (3) for DZD) or solely without reservoir (DZD is defined as a compound event of SPEI48 − 1.5 ∩ SRFI48 − 1.5 ∩ SWSI48 0.6), introduces inconsistencies in the spatial patterns of ToFE, we conducted a sensitivity analysis comparing ToFE patterns (Supplementary Fig. 12). The results reveal that spatial differences are negligible

in most regions. The most noticeable delays are confined to the Mediterranean region, where major reservoirs constructions were completed mid- to late-twentieth century (Supplementary Fig. 6). As climate change influences the onset of compound events, it is critical for decision-makers to revisit the role of existing water infrastructure in future water security planning. The application of FAR greater than 0.99, combined with localized reservoir adjustment of DZD detection, ensures that the global ToFE pattern represents both high attribution confidence and hydrological realism, without introducing methodological biases between grid cells with and without reservoirs.

Thirdly, the estimation of the TRD may influence the ToFE of DZD. The TRD is considered as the duration to take for a multi-compound drought event to dry the water in the reservoirs if the only source of the water supply of the reservoirs is river flow during a drought period. Our approach seems to be reasonable, and we also checked the sensitivity of our assumption by doubling and quadrupling the TRD time scale (Supplementary Fig. 11). The results show that only a few regions have a small change of one decade with increased TRD. However, the TRD is also influenced by various socio-economic factors, such as water demand and the socio-economic sectoral usage, which we address using the Standardized Water Scarcity Index (SWSI48). It is important to note that political decisions regarding management were not included in this modeling approach.

Fourthly, we have looked at the sensitivity of the time scale by considering the 36- and 60-month time scales (Supplementary Figs. 15 and 16) of long-duration compound events for SPEI, SRFI, and SWSI. Only a few regions, located almost entirely in Africa, show changes in ToFE using a 36 or 60-month timescale of extreme events, as shown in Supplementary Fig. 17.

Fifthly, we look at the sensitivity of the ToFE relative to model structure across the CESM2-LE members. We repeat the analysis, looking at the model uncertainty by looking for the ToFE for each member in CESM2-LE, based on the following formulation of FAR below (Eq. (5)). This allows us to examine the spread of emerging timing of Fay Zero Droughts (DZD) and to evaluate the inter-member agreement as shown in Supplementary Fig. 20. The result exhibit, Supplementary Fig. 20a, substantial variability among ensemble members between 1900 and 1990, reflecting high uncertainty during this early period when the anthropogenic signal is still weak relative to internal variability, showing that structural uncertainty arising from the use of a single model remains an important caveat. However, a strong ensemble consensus emerged after 2000, with most members indicating emergence between 2020 and 2030, and increasing agreement toward the end of the twenty-first century. Individual ensemble members (thin green lines) show very synchronized emergence between 2030–2040. There is a sharp, narrow peak, indicating low ensemble spread and high confidence in ToFE under strong forcing. This coherence across members supports the robustness of our findings in terms of both timing and magnitude of anthropogenic influence on DZD events in CESM2-LE under SSP3-7.0.

$$\text{FAR}_i(t) = 1 - \frac{P_{\text{preindustrial}, i}}{P_{\text{forcing}, i}(t)} \text{ with } \begin{cases} P_{\text{preindustrial}, i} = \frac{\text{event}_{\text{preindustrial}, i}(\text{DZD})}{N_{\text{preindustrial}, i}} \\ P_{\text{forcing}, i}(t) = \frac{\text{event}(t)_{\text{forcing}, i}(\text{DZD})}{N_{\text{forcing}, i}(t)} \end{cases} \quad (5)$$

Where $P_{\text{preindustrial}, i}$ is the probability of the counterfactual for member i, which is the ratio between the summation of the event of the DZD event within the preindustrial period (1850-1899) and the number of samples within the same period ($N_{\text{preindustrial}}$). While $P_{\text{forcing}, i}(t)$ is the probability of the factual for member i, which is the ratio between the decadal summation of the frequency of the DZD event of the member i during each decade from 1900 to 2100 and the number of samples during the decade ($N_{\text{forcing}}(t)$). The ToFE of DZD has been considered as the first decade of FAR greater than 0.99, where a 99% probability of the impact of the acute water scarcity that has emerged can be

associated with a human-induced signal after the decade of completion of reservoirs.

Sixthly, to evaluate the influence of model structural uncertainty on the ToFE of DZD events, we extended our analysis beyond CESM2-LE by using hydro-climatic data from the Centre National de Recherche Météorologiques (CNRM) models (SSP2-4.5 and SSP3-7.0 with 1.4 ×1.4 degrees) from the Coupled Model Intercomparison Project Phase 6 (CMIP6). Specifically, we analyzed simulations under the SSP2-4.5 and SSP3-7.0 scenarios, including monthly precipitation, minimum and maximum temperature, and river discharge data spanning 1850-2100. Due to the unavailability of water demand projections under SSP3-7.0, we used water consumption estimates from SSP3-RCP6.0 across the five Global Climate Models (GCMs) from GFDL, HADGEM, IPSL, MIROC, and NORESM, which account for sectoral water use sectors such as domestic, irrigation, industry, electricity, livestock, and mining, capturing socio-economic development water use demand. We applied the same methodology used for CESM2-LE. Computing the three key indicators, the SPEI48, SRFI48, and SWSI48, and applying quantile delta mapping (QDM) bias correction using drought indices ERA5-based references. To ensure methodological consistency and data completeness, we selected 10 ensemble members from the CNRM model that include both atmospheric and river discharge variables across historical and both SSP2-45 and SSP3-7.0 future scenarios: CM6-1 (r2i1p1f2, r3i1p1f2, r4i1p1f2, r5i1p1f2, r6i1p1f2), ESM2-1 (r2i1p1f2, r3i1p1f2, r4i1p1f2, r5i1p1f2), and CM6-1-HR (r1i1p1f2). We use the methods as structured estimates that enable consistent analysis across regions and sectors. The spatial resolution of the datasets is interpolated to the CNRM atmospheric model resolution (1.4° x 1.4°) using the first-order conservative remapping (remapcon) method from the Climate Data Operator[78] (CDO).

The spatial patterns (Supplementary Fig. 21) reveal pronounced inter-model and scenario differences. Results from the CNRM model indicate that, under both SSP2-4.5 and SSP3-7.0 scenarios, 51% of DZD-affected regions are projected to face unprecedented water scarcity by 2100, with 22% experiencing emergence as early as 2020–2030 (Supplementary Fig. 21b, c). Compared to CESM2-LE (Supplementary Fig. 21a), which projects later DZD emergence and a more geographically confined hotspot, especially in the Mediterranean, the United States of America (USA), and Africa, the CNRM model (Supplementary Fig. 21b, c) shows earlier and more widespread emergence. The inter-model comparison (Supplementary Fig. 21d, e) reveals that CESM2-LE and CNRM disagree on the emergence of DZD in 76% of DZD-prone regions, indicating that emergence is detected in only one of the two models in some areas. Notably, 14% of ToFE show later emergence under CESM2-LE (Supplementary Fig. 21d), even under the same forcing scenario (SSP3-7.0), suggesting that CESM2-LE is more conservative in detecting later emergence of compound hydrological extremes. However, CESM2-LE and CNRM agree on DZD occurrence across 24% of the DZD-prone land area, though within this overlap, CESM2-LE projects later emergence over 14% of the area and earlier emergence over 10% compared to CNRM. Moreover, ensemble spread within CNRM (Supplementary Fig. 20b, c) also illustrates the variability among the models to detect the water scarcity. The PDFs of individual members are more dispersed, with multiple peaks and flatter. The thick green line (representing ToFE derived from Eq. (4)) is broader and flatter, indicating the variability in ToFE across ensemble members, reflecting uncertainty in the timing of DZD emergence across members. This variability emphasized the challenge of detecting a robust probabilistic signal from a limited ensemble size. These findings highlight the critical role of model structural differences in shaping projections of hydrological extremes. Importantly, probabilistic attribution methods, such as the FAR, require large ensemble sizes to confidently characterize forced emergence signals. The relatively small ensemble available for CNRM under SSP3-7.0 limits the reliability of such analysis and reinforces the need for larger and more consistent

multi-model ensemble frameworks to assess future water scarcity risks.

Finally, to assess the sensitivity of the ToFE of DZD relative to future socioeconomic scenarios, we applied our detection framework to hydro-climatic simulations from CMIP6 CNRM models under the SSP2-4.5 scenario. We utilized the same ensemble members of the CNRM model to ensure consistency: CM6-1 (r2i1p1f2, r3i1p1f2, r4i1p1f2, r5i1p1f2, r6i1p1f2), ESM2-1 (r2i1p1f2, r3i1p1f2, r4i1p1f2, r5i1p1f2), and CM6-1-HR (r1i1p1f2). The analysis incorporated available water consumption projections from five Global Climate Models (GCMs) from GFDL, HADGEM, IPSL, MIROC, and NORESM under SSP2-RCP4.5. The approach followed the same methodological steps as applied to CESM2-LE (Supplementary Fig. 1). Specifically, we computed the SPEI48, SRFI48, and SWSI48, and applied the bias correction method, QDM, using ERA5-based reference indices, and subsequently determined the ToFE. All datasets are interpolated to the CNRM atmospheric resolution (1.4° × 1.4°) using the first-order conservative remapping (remapcon) method from the CDO. The results (Supplementary Fig. 20c) reveal substantial spread among ensemble members under CNRM SSP2-4.5, highlighting pronounced uncertainty in DZD emergence timing throughout the twenty-first century. Compared to the higher-emission SSP3-7.0 (Supplementary Fig. 20b), the emergence is delayed and more dispersed, with broader PDFs and later peaks, suggesting that moderate forcings lead to slower distribution and less certain emergence of water scarcity extremes. When comparing the special pattern of ToFE under CNRM SSP2-4.5 with CESM2-LE SSP3-7.0 (Supplementary Fig. 21e), results show that high spatial disagreement of 76% of land areas exhibit uncertain DZD emergence, meaning that emergence is detected in only one of the models. Only 9% of regions show earlier emergence in CESM2-LE SSP3-7.0, while 14% indicate later emergence relative to CNRM SSP2-4.5. By considering the same model, CNRM, under different scenarios, SSP3-7.0 and SSP2-4.5 (Supplementary Fig. 21f), the uncertainty still dominates but decreases to 43% of the land area, and spatial discrepancies in DZD-prone regions persist across scenarios. Notably, the near-equal split between earlier and later emergence in different regions indicates that scenario choice (SSP3-7.0 vs. SSP2-4.5) may affect ToFE more symmetrically but also underscores the spatial heterogeneity of hydrological responses to combined climate and water use stress. The results show that the influence of emission scenarios on DZD ToFE is region-specific, due to the interaction between regional climate drivers and human water use. Under the high-emission scenario (SSP3-7.0), DZD emergence can either advance or be delayed depending on the region. Notably, spatial discrepancies in DZD-prone regions persist across scenarios, with 43% of the land area remaining uncertain between the SSP2-4.5 and SSP3-7.0 scenarios within the CNRM model. However, both scenarios, SSP2-4.5 and SSP3-7.0, agree on DZD emergence across 57% of the DZD-prone land area. Within this overlap, SSP3-7.0 projects later emergence over 17% of the area and earlier emergence over 18% compared to SSP2-4.5, while 22% of the area shows no change in the ToFE between the two scenarios (Supplementary Fig. 21f). These findings underscore the role of both scenario and model structures in shaping DZD emergence. Notably, even under high-forcing SSP3-7.0, CESM2-LE may still project later ToFE than CNRM under moderate forcing (SSP2-4.5), pointing to differences in model sensitivity to hydro-climatic stressors. This highlights the importance of multi-model and multi-scenario assessments when evaluating risks associated with extreme emergence and water scarcity. Furthermore, a probabilistic approach such as the FAR requires large ensembles to ensure robust estimates. The relatively small ensemble size of CNRM limits the confidence in scenario-attribution results, underscoring the need for ensemble expansion and multi-model convergence to improve attribution robustness and risk quantification. Given these model differences, CESM2-LE provides output at a higher spatial resolution (1.25° × 0.9375°)

compared to the lower-resolution CNRM model (1.40625° × 1.40625°). CESM2-LE detects finer-scale features and localized extremes that may be overlooked or underrepresented in the CNRM. Therefore, we have not aggregated events across both CESM2-LE and CNRM, since increasing the CNRM resolution to the resolution of CESM2-LE could introduce spatial biases and distort the representation of extreme events.

Data availability

All datasets are freely accessible to the public. The CESM2-LE data can be accessed at: https://www.cesm.ucar.edu/community-projects/lens2, retrieved in August 2022. The ECMWF Reanalysis v5 (ERA5-Land) data can be found at https://cds.climate.copernicus.eu. The GloFAS-ERA5 dataset was downloaded from https://ewds.climate.copernicus.eu/datasets/cems-glofas-historical?tab=overview with the DOI: 10.24381/cds.a4fdd6b9, updated in February 2025. The reservoir data are available at https://www.globaldamwatch.org/grand, accessed in December 2023. The HYDE population data can be found at https://public.yoda.uu.nl/geo/UU01/94FNH0.html, retrieved in May 2024. The downscaling Global Spatial Population Projections from 1/8-degree to 1-km Grid Cells from NCAR is available at: https://www.cgd.ucar.edu/sections/iam/modeling/spatial-population, consulted in August 2022. The monthly sectoral water demand data used in this study are available via https://dataverse.harvard.edu/dataset.xhtml?persistentId=doi:10.7910/DVN/VIQEAB, assessed in July 2024. The CNRM-CERFACS data (SSP2.4-5 and SSP3.7-0) are available online from the Earth System Grid Federation (ESGF) public data repository (https://aims2.llnl.gov/search/?project=CMIP6/), assessed in July 2025.

Code availability

The data for this study were analyzed using R, and the figures were generated using Python under Spyder with publicly available tool packages. The available open-source packages comprise: spei.R (https://rdrr.io/cran/SPEI/src/R/spei.R), MBC-QDM.R (https://rdrr.io/cran/MBC/src/R/MBC-QDM.R), drc (https://rdrr.io/cran/drc/). The scripts for the data analysis are available from the GitHub and Zenodo repositories[111] at https://github.com/phyvera/ToFE_DZD and https://doi.org/10.5281/zenodo.16723000.

References

1. Wolski, P. How severe is Cape Town's "Day Zero" drought? *Significance*. **15**, 24–27 (2018).
2. Holden, P. B. et al. Nature-based solutions in mountain catchments reduce impact of anthropogenic climate change on drought streamflow. *Commun. Earth Environ.* **3**, 51 (2022).
3. Botai, C., Botai, J., De Wit, J., Ncongwane, K. & Adeola, A. Drought characteristics over the Western Cape Province, South Africa. *Water* **9**, 876 (2017).
4. Booysen, M. J., Visser, M. & Burger, R. Temporal case study of household behavioural response to Cape Town's "Day Zero" using smart meter data. *Water Res.* **149**, 414–420 (2019).
5. Oluwatayo, I. B. & Braide, T. M. Socioeconomic determinants of households' vulnerability to drought in Western Cape, South Africa. *Sustainability* **14**, 7582 (2022).
6. State of Cape Town Report. Research Branch of the City's Policy and Strategy Department in the Future Planning and Resilience Directorate. City of Cape Town. Collated by Aaishah Petersen, with inputs from Jameyah Armien, Sivuyile Rilityana, Ndileka Makohliso and Mojalefa Makitle. https://resource.capetown.gov.za/documentcentre/Documents/City%20research%20reports%20and%20review/State_Of_Cape_Town_Report_2022.pdf (2022).
7. Kalia, B. Water crisis in cities: the case of 'Day Zero' in Chennai, India. https://ic-sd.org/wp-content/uploads/2020/11/Bhrigu-Kalia.pdf (2020).
8. Pincetl, S. et al. Adapting urban water systems to manage scarcity in the 21st century: the case of Los Angeles. *Environ. Manage.* **63**, 293–308 (2019).
9. Liu, J., Liu, Q. & Yang, H. Assessing water scarcity by simultaneously considering environmental flow requirements, water quantity, and water quality. *Ecol. Indic.* **60**, 434–441 (2016).
10. Hao, Z., Singh, V. & Hao, F. Compound extremes in hydroclimatology: a review. *Water* **10**, 718 (2018).
11. Zscheischler, J. et al. Future climate risk from compound events. *Nat. Clim. Change* **8**, 469–477 (2018).
12. IPCC. Managing the Risks of Extreme Events and Disasters to Advance Climate Change Adaptation. *A Special Report of Working Groups I and II of the Intergovernmental Panel on Climate Change* (eds. Field, C. B. et al.) 582 (Cambridge University Press, Cambridge, UK, and New York, NY, USA, 2012).
13. Zscheischler, J., Van Den Hurk, B., Ward, P. J. & Westra, S. Multivariate extremes and compound events. In *Climate Extremes and Their Implications for Impact and Risk Assessment* (eds. Sillmann, J., Sippel, S. & Russo, S.) 59–76 (Elsevier, 2020). https://doi.org/10.1016/B978-0-12-814895-2.00004-5.
14. Cárdenas Belleza, G. A., Bierkens, M. F. P. & Van Vliet, M. T. H. Sectoral water use responses to droughts and heatwaves: analyses from local to global scales for 1990–2019. *Environ. Res. Lett.* **18**, 104008 (2023).
15. Allen, C. D., Breshears, D. D. & McDowell, N. G. On underestimation of global vulnerability to tree mortality and forest die-off from hotter drought in the Anthropocene. *Ecosphere* **6**, 1–55 (2015).
16. Douville, H. et al. & Intergovernmental Panel on Climate Change (IPCC). Water cycle changes. In *Climate Change 2021: The Physical Science Basis. Contribution of Working Group I to the Sixth Assessment Report of the Intergovernmental Panel on Climate Change* (Cambridge University Press, 2021).
17. Yoon, J.-H. et al. Increasing water cycle extremes in California and in relation to ENSO cycle under global warming. *Nat. Commun.* **6**, 8657 (2015).
18. Dai, A., Zhao, T. & Chen, J. Climate change and drought: a precipitation and evaporation perspective. *Curr. Clim. Change Rep.* **4**, 301–312 (2018).
19. Vörösmarty, C. J., Green, P., Salisbury, J. & Lammers, R. B. Global water resources: vulnerability from climate change and population growth. *Science* **289**, 284–288 (2000).
20. Dai, A. Drought under global warming: a review. *WIREs Clim. Change* **2**, 45–65 (2011).
21. Dai, A. Increasing drought under global warming in observations and models. *Nat. Clim. Change* **3**, 52–58 (2013).
22. Vicente-Serrano, S. M. et al. Global characterization of hydrological and meteorological droughts under future climate change: the importance of timescales, vegetation-CO2 feedbacks and changes to distribution functions. *Int. J. Climatol.* **40**, 2557–2567 (2020).
23. Van Loon, A. F. et al. Drought in the Anthropocene. *Nat. Geosci.* **9**, 89–91 (2016).
24. Van Vliet, M. T. H. et al. Global water scarcity including surface water quality and expansions of clean water technologies. *Environ. Res. Lett.* **16**, 024020 (2021).
25. Veldkamp, T. I. E. et al. Changing mechanism of global water scarcity events: Impacts of socioeconomic changes and interannual hydro-climatic variability. *Glob. Environ. Change* **32**, 18–29 (2015).
26. Veldkamp, T. I. E. et al. Water scarcity hotspots travel downstream due to human interventions in the 20th and 21st century. *Nat. Commun.* **8**, 15697 (2017).
27. Mekonnen, M. M. & Hoekstra, A. Y. Four billion people facing severe water scarcity. *Sci. Adv.* **2**, e1500323 (2016).

28. Wang, M. et al. A triple increase in global river basins with water scarcity due to future pollution. *Nat. Commun.* **15**, 880 (2024).

29. He, C. et al. Future global urban water scarcity and potential solutions. *Nat. Commun.* **12**, 4667 (2021).

30. Dube, K., Nhamo, G. & Chikodzi, D. Climate change-induced droughts and tourism: impacts and responses of Western Cape province, South Africa. *J. Outdoor Recreat. Tour.* **39**, 100319 (2022).

31. Brühl, J. & Visser, M. The Cape Town drought: a study of the combined effectiveness of measures implemented to prevent "Day Zero. *Water Resour. Econ.* **34**, 100177 (2021).

32. Burls, N. J. et al. The Cape Town "Day Zero" drought and Hadley cell expansion. *Npj Clim. Atmos. Sci.* **2**, 27 (2019).

33. Pascale, S., Kapnick, S. B., Delworth, T. L. & Cooke, W. F. Increasing risk of another Cape Town "Day Zero" drought in the 21st century. *Proc. Natl. Acad. Sci. USA* **117**, 29495–29503 (2020).

34. Roffe, S. J., Steinkopf, J. & Fitchett, J. M. South African winter rainfall zone shifts: a comparison of seasonality metrics for Cape Town from 1841–1899 and 1933–2020. *Theor. Appl. Climatol.* **147**, 1229–1247 (2022).

35. Odoulami, R. C., Wolski, P. & New, M. A SOM-based analysis of the drivers of the 2015–2017 Western Cape drought in South Africa. *Int. J. Climatol.* **41**, E1518–E1530 (2021).

36. Otto, F. E. L. et al. Anthropogenic influence on the drivers of the Western Cape drought 2015–2017. *Environ. Res. Lett.* **13**, 124010 (2018).

37. Odoulami, R. C., Wolski, P. & New, M. Attributing the driving mechanisms of the 2015–2017 drought in the Western Cape (South Africa) using self-organising maps. *Environ. Res. Lett.* **18**, 074043 (2023).

38. Satoh, Y. et al. The timing of unprecedented hydrological drought under climate change. *Nat. Commun.* **13**, 3287 (2022).

39. Liu, J. et al. Timing the first emergence and disappearance of global water scarcity. *Nat. Commun.* **15**, 7129 (2024).

40. Akbas, A., Freer, J., Ozdemir, H., Bates, P. D. & Turp, M. T. What about reservoirs? Questioning anthropogenic and climatic interferences on water availability. *Hydrol. Process.* **34**, 5441–5455 (2020).

41. Di Baldassarre, G., Martinez, F., Kalantari, Z. & Viglione, A. Drought and flood in the Anthropocene: feedback mechanisms in reservoir operation. *Earth Syst. Dyn.* **8**, 225–233 (2017).

42. Di Baldassarre, G. et al. Water shortages worsened by reservoir effects. *Nat. Sustain.* **1**, 617–622 (2018).

43. Qi, Y. et al. Future changes in drought frequency due to changes in the mean and shape of the PDSI probability density function under RCP4.5 scenario. *Front. Earth Sci.* **10**, 857885 (2022).

44. Best, J. Anthropogenic stresses on the world's big rivers. *Nat. Geosci.* **12**, 7–21 (2019).

45. Prudhomme, C. et al. Hydrological droughts in the 21st century, hotspots and uncertainties from a global multimodel ensemble experiment. *Proc. Natl. Acad. Sci. USA* **111**, 3262–3267 (2014).

46. Vieira, M. J. F. & Stadnyk, T. A. Leveraging global climate models to assess multi-year hydrologic drought. *Npj Clim. Atmos. Sci.* **6**, 179 (2023).

47. Lu, W. et al. Hydrological projections of future climate change over the source region of Yellow River and Yangtze River in the Tibetan Plateau: a comprehensive assessment by coupling RegCM4 and VIC model. *Hydrol. Process.* **32**, 2096–2117 (2018).

48. Kraaijenbrink, P. D. A., Stigter, E. E., Yao, T. & Immerzeel, W. W. Climate change decisive for Asia's snow meltwater supply. *Nat. Clim. Change* **11**, 591–597 (2021).

49. Gu, H. et al. Impact of climate change on hydrological extremes in the Yangtze River Basin, China. *Stoch. Environ. Res. Risk Assess.* **29**, 693–707 (2015).

50. Hirabayashi, Y. et al. Global flood risk under climate change. *Nat. Clim. Change* **3**, 816–821 (2013).

51. Giuntoli, I., Vidal, J.-P., Prudhomme, C. & Hannah, D. M. Future hydrological extremes: the uncertainty from multiple global climate and global hydrological models. *Earth Syst. Dyn.* **6**, 267–285 (2015).

52. Hanasaki, N. et al. A global water scarcity assessment under Shared Socio-economic Pathways—part 2: water availability and scarcity. *Hydrol. Earth Syst. Sci.* **17**, 2393–2413 (2013).

53. Matthews, J. H. Climate policy is inundating the SDGs. *Nat. Water* **1**, 216–218 (2023).

54. United Nations. Sustainable Development Gal 6 Synthesis Report 2018 on water and Sanitation. (New York, 2018), https://www.gwp.org/contentassets/d57b65ff36804dbcb6a8ff98abe8214a/sdg-6-synthesis-report-2018-on-water-and-sanitation.pdf.

55. Rockström, J., Mazzucato, M., Andersen, L. S., Fahrländer, S. F. & Gerten, D. Why we need a new economics of water as a common good. *Nature* **615**, 794–797 (2023).

56. Pisor, A. C. et al. Effective climate change adaptation means supporting community autonomy. *Nat. Clim. Change* **12**, 213–215 (2022).

57. Basheer, M. et al. Cooperative adaptive management of the Nile River with climate and socio-economic uncertainties. *Nat. Clim. Change* **13**, 48–57 (2023).

58. Jiménez, A. et al. Unpacking water governance: a framework for practitioners. *Water* **12**, 827 (2020).

59. Becher, O. et al. The challenge of closing the climate adaptation gap for water supply utilities. *Commun. Earth Environ.* **5**, 356 (2024).

60. Orth, R., Zscheischler, J. & Seneviratne, S. I. Record dry summer in 2015 challenges precipitation projections in Central Europe. *Sci. Rep.* **6**, 28334 (2016).

61. Denissen, J. M. C. et al. Widespread shift from ecosystem energy to water limitation with climate change. *Nat. Clim. Change* **12**, 677–684 (2022).

62. Kuang, X. et al. The changing nature of groundwater in the global water cycle. *Science* **383**, eadf0630 (2024).

63. Jasechko, S. & Perrone, D. Global groundwater wells at risk of running dry. *Science* **372**, 418–421 (2021).

64. Liu, P.-W. et al. Groundwater depletion in California's Central Valley accelerates during megadrought. *Nat. Commun.* **13**, 7825 (2022).

65. Van Loon, A. F. & Van Lanen, H. A. J. A process-based typology of hydrological drought. *Hydrol. Earth Syst. Sci.* **16**, 1915–1946 (2012).

66. Raymond, C. et al. Understanding and managing connected extreme events. *Nat. Clim. Change* **10**, 611–621 (2020).

67. Stolte, T. R. et al. Global drought risk in cities: present and future urban hotspots. *Environ. Res. Commun.* **5**, 115008 (2023).

68. Torelló-Sentelles, H. & Franzke, C. L. E. Drought impact links to meteorological drought indicators and predictability in Spain. *Hydrol. Earth Syst. Sci.* **26**, 1821–1844 (2022).

69. Calverley, C. M. & Walther, S. C. Drought, water management, and social equity: analyzing Cape Town, South Africa's water crisis. *Front. Water* **4**, 910149 (2022).

70. Miyan, M. A. Droughts in Asian least developed countries: vulnerability and sustainability. *Weather Clim. Extrem.* **7**, 8–23 (2015).

71. Rosa, L., Chiarelli, D. D., Rulli, M. C., Dell'Angelo, J. & D'Odorico, P. Global agricultural economic water scarcity. *Sci. Adv.* **6**, eaaz6031 (2020).

72. Rodgers, K. B. et al. Ubiquity of human-induced changes in climate variability. https://esd.copernicus.org/preprints/esd-2021-50/esd-2021-50.pdf, https://doi.org/10.5194/esd-2021-50 (2021).

73. Lehner, B. et al. High-resolution mapping of the world's reservoirs and dams for sustainable river-flow management. *Front. Ecol. Environ*. **9**, 494–502 (2011).

74. Li, Y., Zhao, G., Allen, G. H. & Gao, H. Diminishing storage returns of reservoir construction. *Nat. Commun*. **14**, 3203 (2023).

75. Grill, G. et al. An index-based framework for assessing patterns and trends in river fragmentation and flow regulation by global dams at multiple scales. *Environ. Res. Lett*. **10**, 015001 (2015).

76. Khan, Z. et al. Global monthly sectoral water use for 2010–2100 at 0.5° resolution across alternative futures. *Sci. Data* **10**, 201 (2023).

77. Ritz, C., Baty, F., Streibig, J. C. & Gerhard, D. Dose-response analysis using R. *PLoS ONE* **10**, e0146021 (2015).

78. Schulzweida, U. CDO user guide. https://doi.org/10.5281/ZENODO.10020800 (2023).

79. Klein Goldewijk, K., Beusen, A., Doelman, J. & Stehfest, E. Anthropogenic land use estimates for the Holocene—HYDE 3.2. *Earth Syst. Sci. Data* **9**, 927–953 (2017).

80. Gao, J. Downscaling global spatial population projections from 1/8-degree to 1-km grid cells. https://opensky.ucar.edu/islandora/object/technotes:553 (2017).

81. Bae, S., Lee, S.-H., Yoo, S.-H. & Kim, T. Analysis of drought characteristics using time series of modified SPEI in South Korea from 1981 to 2010. http://www.preprints.org/manuscript/201610.0013/v1 (2016).

82. Kim, B. S., Chang, I. G., Sung, J. H. & Han, H. J. Projection in future drought hazard of South Korea based on RCP climate change scenario 8.5 using SPEI. *Adv. Meteorol*. **2016**, 1–23 (2016).

83. Li, W. et al. Future changes in the frequency of extreme droughts over China based on two large ensemble simulations. *J. Clim*. 6023–6035. https://doi.org/10.1175/JCLI-D-20-0656.1 (2021).

84. Li, X. et al. Concurrent droughts and hot extremes in northwest China from 1961 to 2017. *Int. J. Climatol*. **39**, 2186–2196 (2019).

85. Mallya, G., Mishra, V., Niyogi, D., Tripathi, S. & Govindaraju, R. S. Trends and variability of droughts over the Indian monsoon region. *Weather Clim. Extrem*. **12**, 43–68 (2016).

86. Naumann, G., Spinoni, J., Vogt, J. V. & Barbosa, P. Assessment of drought damages and their uncertainties in Europe. *Environ. Res. Lett*. **10**, 124013 (2015).

87. Zhao, M., A, G., Liu, Y. & Konings, A. G. Evapotranspiration frequently increases during droughts. *Nat. Clim. Change* **12**, 1024–1030 (2022).

88. Vicente-Serrano, S. M., Beguería, S. & López-Moreno, J. I. A multiscalar drought index sensitive to global warming: the standardized precipitation evapotranspiration index. *J. Clim*. **23**, 1696–1718 (2010).

89. Droogers, P. & Allen, R. G. Estimating reference evapotranspiration under inaccurate data conditions. *Irrig. Drain. Syst*. **16**, 33–45 (2002).

90. Vicente-Serrano, S. M. et al. Performance of drought indices for ecological, agricultural, and hydrological applications. *Earth Interact* **16**, 1–27 (2012).

91. Lorenzo-Lacruz, J. et al. The impact of droughts and water management on various hydrological systems in the headwaters of the Tagus River (central Spain). *J. Hydrol*. **386**, 13–26 (2010).

92. Li, Z. et al. Clarifying the propagation dynamics from meteorological to hydrological drought induced by climate change and direct human activities. *J. Hydrometeorol*. https://doi.org/10.1175/JHM-D-21-0033.1 (2021).

93. Van Loon, A. F. Hydrological drought explained. *WIREs Water* **2**, 359–392 (2015).

94. Vereecken, H. et al. Soil hydrology in the Earth system. *Nat. Rev. Earth Environ*. **3**, 573–587 (2022).

95. Shukla, S. & Wood, A. W. Use of a standardized runoff index for characterizing hydrologic drought. *Geophys. Res. Lett*. **35**, 2007GL032487 (2008).

96. Vicente-Serrano, S. M. et al. Accurate computation of a streamflow drought index. *J. Hydrol. Eng*. **17**, 318–332 (2012).

97. Beguería, S. & Vicente-Serrano, S. M. SPEI: Calculation of the Standardized Precipitation-Evapotranspiration Index. 1.8.1 https://doi.org/10.32614/CRAN.package.SPEI (2011).

98. Huang, L. & Yin, L. Supply and demand analysis of water resources based on system dynamics model. *J. Eng. Technol. Sci*. **49**, 705–720 (2017).

99. Ansari, R., Casanueva, A., Liaqat, M. U. & Grossi, G. Evaluation of bias correction methods for a multivariate drought index: case study of the Upper Jhelum Basin. *Geosci. Model Dev*. **16**, 2055–2076 (2023).

100. Van De Velde, J., Demuzere, M., De Baets, B. & Verhoest, N. E. C. Impact of bias nonstationarity on the performance of uni- and multivariate bias-adjusting methods: a case study on data from Uccle, Belgium. *Hydrol. Earth Syst. Sci*. **26**, 2319–2344 (2022).

101. Cannon, A. J., Sobie, S. R. & Murdock, T. Q. Bias correction of GCM precipitation by quantile mapping: how well do methods preserve changes in quantiles and extremes? *J. Clim*. **28**, 6938–6959 (2015).

102. Li, H., Sheffield, J. & Wood, E. F. Bias correction of monthly precipitation and temperature fields from Intergovernmental Panel on Climate Change AR4 models using equidistant quantile matching. *J. Geophys. Res. Atmos*. **115**, 2009JD012882 (2010).

103. Wang, L. & Chen, W. Equiratio cumulative distribution function matching as an improvement to the equidistant approach in bias correction of precipitation. *Atmos. Sci. Lett*. **15**, 1–6 (2014).

104. Intergovernmental Panel on Climate Change (IPCC). *Managing the Risks of Extreme Events and Disasters to Advance Climate Change Adaption: Special Report of the Intergovernmental Panel on Climate Change* (Cambridge University Press, 2012).

105. Perkins-Kirkpatrick, S. E. et al. On the attribution of the impacts of extreme weather events to anthropogenic climate change. *Environ. Res. Lett*. **17**, 024009 (2022).

106. Black, M. T., Karoly, D. J. & King, A. D. The contribution of anthropogenic forcing to the Adelaide and Melbourne, Australia, Heat Waves of January 2014. *Bull. Am. Meteorol. Soc*. **96**, S145–S148 (2015).

107. Kirchmeier-Young, M. C., Gillett, N. P., Zwiers, F. W., Cannon, A. J. & Anslow, F. S. Attribution of the influence of human-induced climate change on an extreme fire season. *Earths Future* **7**, 2–10 (2019).

108. Zhong, S., Ying, J. & Collins, M. Sources of uncertainty in the time of emergence of tropical Pacific climate change signal: role of internal variability. *J. Clim*. **36**, 2535–2549 (2023).

109. Mora, C. et al. The projected timing of climate departure from recent variability. *Nature* **502**, 183–187 (2013).

110. Batibeniz, F., Hauser, M. & Seneviratne, S. I. Countries most exposed to individual and concurrent extremes and near-permanent extreme conditions at different global warming levels. *Earth Syst. Dyn*. **14**, 485–505 (2023).

111. Ravinandrasana, V. P. & Franzke, C. L. E. The first emergence of unprecedented global water scarcity in the anthropocene, phy-vera/ToFE_DZD: ToFE_DZD. https://doi.org/10.5281/zenodo.16723000 (2025).

Acknowledgements

Author contributions

V.P.R. and C.L.E.F. jointly designed the study and contributed to the writing of the paper as well as the interpretation of the results. V.P.R. collected data, performed the calculations and statistical analyses, prepared the figures, and drafted the article.

Competing interests

The authors declare no competing interests.

Additional information

Supplementary information The online version contains supplementary material available at
https://doi.org/10.1038/s41467-025-63784-6.

Correspondence and requests for materials should be addressed to Christian L. E. Franzke.

Peer review information *Nature Communications* thanks Rene Orth and the other anonymous reviewer(s) for their contribution to the peer review of this work. A peer review file is available.

Reprints and permissions information is available at
http://www.nature.com/reprints

Publisher's note Springer Nature remains neutral with regard to jurisdictional claims in published maps and institutional affiliations.